SLAC-PUB-3180
29 September 1983
(I)

The MARK III Time-of-Flight System*

J. S. BROWN, T. H. BURNETT, V. COOK,
C. DEL PAPA[1], A. L. DUNCAN, P. M. MOCKETT,
J. C. SLEEMAN, H-J. WILLUTZKI.
University of Washington
Seattle, WA 98195

and

D. E. WISINSKI
Stanford Linear Accelerator Center
Stanford University, Stanford, California 94305

Submitted to Nuclear Instruments and Methods

ABSTRACT

The MARK III time-of-flight system comprises 48 scintillation counters 5 cm thick, mounted parallel to the beam axis at a radius of 1.18 m, and covering 80% of the total solid angle. The mean resolution is 170–190 psec (depending on particle type), which provides π/K discrimination up to 1.2 GeV/c at 2σ separation .

---

* Work supported by the Department of Energy, contract DE-AC03-76SF00515

Present Addresses

1. INFN Sezione di Bologna, Bologna, Italy.

1. Introduction

This paper describes the time-of-flight counters of the MARK III detector at SPEAR and summarizes their performance on data taken during the Spring of 1983.

The detector is shown in transverse and axial cross section in Figs.1and 2. All components other than the ToF system are described elsewhere[1] .

The resolution of the system as a whole determines the range of momentum for which particle indentification is possible. However, it contains contributions from three distinct sources. The dominant one is the intrinsic time resolution of the counters, but the others, from the tracking resolution in the drift chamber and the jitter of the time-reference, are not negligible.

2. General Description of the Counters

The system comprises 48 counters, mounted on the cylindrical drift chamber and parallel to its axis – like the staves of a barrel. The counters subtend a solid angle of 79.8% of 4π steradians. They are held in place by tensioned stainless steel bands pressing on aluminum plates cushioned by rubber sheets, as shown in Fig.3 . The counters are separated from the aluminum skin of the drift chamber by a centimeter of styrofoam glued to it and planed longitudinally so as to have the cross section of a regular 48-sided polygon with an inscribed radius of 1.15 m. Thus each counter rests on a flat surface; this prevents slipping and distributes the load evenly.

Fig.4 shows an individual counter. The scintillator is 5.1 cm thick, 15.6 cm wide and 317.5 cm long. The thickness was chosen as a compromise between the need to maximize the number of produced photons and the limited space available between the drift chamber and the barrel shower counter. The edges are angled such that the faces of adjacent counters are plane-parallel and have gaps of about 1 mm between them. The counters enclose a volume of almost uniform magnetic field of 4 kG, and thus particles would need a momentum greater than 3 GeV/c to pass between a pair without traversing any scintillator.

This substantially exceeds the momentum at which the ToF system can identify particle types. The magnetic field also imposes a lower limit of about 80 MeV/c on the transverse momentum of a track that can reach the counters.

The scintillators were cast by Nuclear Enterprises to the designed shape, thus avoiding any machining of surfaces, in order to reduce crazing and surface unevenness.

The scintillator is Nuclear Enterprises Pilot F (specifications in Table 1), and the guide is made of ultraviolet-transmitting (uvt) plexiglass. They are bonded together by NE581 epoxy. Usually this made an excellent optical joint, but a few broke after installation. In a test the effect of this was found to be a loss of less than 20% of light with an increase of less than 10% time resolution.

Table 1 — Specifications of Pilot F Scintillator.

Density	1.032 gm/cm^3
Refractive index	1.58
Decay constant of main component	2.1 nsec
Wavelength of maximum emission	425 nm

Particles passing perpendicularly through the counters traverse 5.3 gm of material, or 12% of a radiation length.

The shape of the light guide was dictated by the need for it to pass through holes in the iron yoke of the magnet with the largest possible area while allowing enough iron for the magnetic return path. Therefore it was tapered from a width of 15.6 cm where it joined the scintillator to half that value where it passed through the iron. The same area was then maintained to within a short distance of the photomultiplier in order to produce the least time-dispersion of the leading photons at the photocathode. The final few centimeters of the guide were turned to cones, matching the diameter of the photocathode. The guides are asymmetrical, so that adjacent pairs of counters have their guides in contact

on one side as shown in Fig.3 . This halves the number of holes needed in the magnet return yoke.

The counters are wrapped in matt black paper and covered with heavy black vinyl Scotch tape. Tests with a nitrogen pulser showed no difference in time resolution if aluminum foil were used instead. The advantages of paper derive mainly from the ease and convenience of use.

The photomultipliers used are Amperex XP2020, whose specifications are listed in Table 2.

Table 2 — Characteristics of the XP2020 Photomultiplier.

Quantum efficiency at 401 nm	26%
Spectral sensitivity at 401 nm	85 mA/W
Gain at 2200 V	3×10^7
Anode pulse rise time	1.5 nsec
Transit time variation	0.25 nsec

Each photomultiplier is attached to the light guide by a 3 mm thick disk of soft transparent material [1] which forms a good mechanical and optical contact. This disk was glued to the light guide and the photomultiplier by Dow Corning transparent RTV. This arrangement is advantageous compared to a solid glue joint, an air-gap, or optical grease. Tests showed no loss of light transmission compared to a joint of optical cement, and the strength and flexibility of the material made assembly much easier, given the tight tolerances of the design.

The photomultipliers are protected magnetically by two concentric mu-metal cylinders, outside of which is a soft-iron tube 6mm thick. It was possible to vary the position of the shielding to obtain a minimum field at the photocathode (whose position was fixed). The field at the position of the photocathode was

[1] 40 parts of Dow Corning Sylgard 184, 1 part 184 hardener, and 3 parts of Dow Corning 200.

measured to be about 0.1 G with the shielding installed. The measurements indicated little advantage from the second mu-metal cylinder, but it was used for additional safety. The iron cylinders are bolted onto a gas manifold, and provide support for the photomultiplier base, thus reducing mechanical stress on the optical joints.

The circuit of the photomultiplier base is shown in Fig.5. The voltages of the accelerating grid and second dynode were adjusted for maximum pulse height, which tests showed gives the best time resolution. The voltages on the photomultipliers range between 1.8 kV and 2.5 kV and the pulses are in the range of 0–2000 pC.

The cables from the detector to the electronics are 75 m long. For most of their length the anode cables (RG215, 50 Ω) [2] , are thermally insulated, partly by foam rubber sheathes and partly by air-conditioned trays. Only the last 2 m are in the open air. They also have a second outer ground shield.

The system is monitored by a pulsed nitrogen laser [3] which feeds ultraviolet light at 337 nm to the center of all counters via 200 μm quartz fibers [4] at hourly intervals while taking data. According to the manufacturer's specifications, the laser delivers 80 μJ of light per pulse, at the specified operating conditions, with pulses approximately 300 psec long. Owing to the shortness of the laser pulse, the output of the photomultiplier is similar to that obtained when a particle hits a counter.

A time reference is obtained by diverting a small fraction of the laser light (with an unsilvered quartz sheet) to a vacuum photodiode [5] . The output of this

---

[2]Dielectric constant varies by about one part in 10^4 per degree C.

[3]Nitromite model LN103 from Photochemical Research Associates, 45 Meg Drive, London, Ontario. This model is also in use in other SLAC experiments.

[4]Fabricated by Belling and Lee (England), from a special high quality batch of QSF200 fiber manufactured by Quartz et Silice (France). These fibers are identical with those used by the CERN experiment UA1, whose requirements for uniformity were much more stringent than those for MARK III.

[5]ITT type F4000 with S5 photocathode.

is transmitted to the electronics and multiplexed with two other time-reference signals described later. From measurements of the amplitude of the photodiode signal it is found that the stability of the laser over a few hours is $\pm 5\%$.

The fibers are coupled to the counters by small prisms [6] of uvt plexiglass glued to the center of the outside surface of the scintillator. These reflect the light, which emerges from the fiber in a narrow cone, down into the scintillator. The fibers pass through stainless steel tubes, which run along the surface of the counters outside the wrapping, and abut the prisms as shown in Fig.6. The fibers are then routed back to the laser through individual plastic conduits with detachable mountings at the counter; near the laser they are gathered into a single steel conduit. This allows for replacement of broken fibers, and the loss of light owing to the small air gap between the end of the fiber and the prism is unimportant because the intensity delivered to the counters is adjusted to the desired value.

The ends of the fibers are protected by small metal ferrules, as shown in Fig.7. These protect the ends both from casual damage and from chipping at the edges during the polishing. Examination of samples under a low-power microscope showed surfaces of high quality.

In order to assure uniform illumination of all the fibers several diffusing quartz plates are placed between the laser and the input ends of the fibers which are gathered into a matrix about 1 cm in diameter. Fig.8 shows the arrangement. Different intensities can be selected by inserting absorbers in the beam, in order to simulate the range of intensities produced by particles.

The fibers were the last components installed in MARK III, because they are the most fragile. However there was considerable difficulty because the ends of the detector had become very crowded. Several repairs and modifications have since been made to the detector, and some fibers were damaged and had to be replaced. This experience suggests that a better procedure might have been to install the fibers earlier in much more heavily protected conduits.

---

[6] The prisms are also similar in design to those used by UA1.

3. Electronics

This experiment uses a CAMAC-based system designed at SLAC. An almost identical configuration was previously used by the MARKII detector[2] at SPEAR and now at PEP.

The system can be considered in two sections.

3.1 Analog Electronics.

This is shown schematically in Fig.9 . It comprises a system of discriminators and time-to-amplitude converters (TACs) mounted in two CAMAC crates, and a NIM discriminator ("3-FLAVOR") that provides the common time reference. These units are described below.

3-FLAVOR MODULE. This is a discriminator[3] which provides very accurate timing from the beam bunches themselves via a pickup in the SPEAR beam-pipe (the "beam-crossing" signal). It is able to handle extremely fast rise times and to compensate for variations of pulse height, providing stability to a few picoseconds. Its input comes via a coaxial multiplexer, which can also switch in signals from the calibration or monitoring circuits when necessary. Its output (NIM) is fanned out to the STROBERs (see below). The unit is gated by the SPEAR r.f. power in order to select the electron bunches as the timing reference.

DISCO. This is a four-channel discriminator and TAC, which measures the times of the photomultiplier pulses at two computer-controlled thresholds as well as the total charges of the pulses. It employs sample-and-hold circuits which are interrogated by the BADC (see below) when an event trigger occurs. The least count of the timing circuit corresponds to approximately 15 psec, and the resolution is about 10 psec. Each unit also stores a measure of the internal temperature of the circuit, which can be used in temperature corrections of the results if necessary. The timing circuit is gated by a pulse from the STROBER, the trailing edge of which provides a common stop for the time measurement. The charge integration circuit is gated by a signal from the THRESHER (see below), via the CAMAC backplane.

The outputs are gated to a common bus to the analog input of the BADC, and the DISCOs are read out sequentially. Each DISCO provides four groups of two times and a charge (one such group per photomultiplier [7]) followed by a measure of its own internal temperature. The busses from the two crates are multiplexed to the BADC by the SPORT module (see below).

The two thresholds are presently used as alternatives, to extend the range of pulse heights for which a good time resolution is possible using a single threshold. However they also contain information on the pulse shape which could conceivably be used to further improve the resolution.

In a test using laser pulses (Fig. 10), which simulate particle data, the range of linearity of the charge measurement was found to be less than the full dynamic range of the unit, and for the largest pulses there was complete saturation. Therefore the voltages of the photomultipliers are adjusted so that the charges should lie within the linear region for most pulses. However, when the test was repeated using longer pulses, from a mercury pulser (used in the on-line calibration), the charge measurement was found to be nearly linear over the whole dynamic range.

The TACs essentially consist of sample-and-hold circuits whose capacitors rest at a constant 5 V until a threshold discriminator starts a discharge through a resistance. The discharge is stopped by the trailing edge of the timing gate, and the charge is held. The capacitors are sensitive to previous voltage settings as the dielectric has a "memory" with a comparatively long relaxation time. So, after the contents of the DISCOs have been read out by the BADC, they must be reset and held at 5 V long enough for the dielectric to relax. This RESET signal is provided by the control logic via the THRESHER. The use of common-stop (rather than common-start) timing ensures that on average the capacitors spend most of the time at a constant voltage, which minimizes the "memory" of previous measurements thus improving resolution.

The circuits of the DISCOs vary slightly in response and are somewhat non-linear. Therefore it is necessary to calibrate them, which is done on-line. Further

---

[7]In any one event, only a few of these correspond to photomultiplier hits.

off-line calibration is needed to deal with effects in the rest of the system. Both these calibration procedures are described in detail later.

THRESHER. This sets two discriminator thresholds, under computer control, for all the DISCOs in one CAMAC crate. The threshold voltages are transmitted via the CAMAC backplane. The THRESHER is also on the analog bus and its instantaneous threshold settings can be read by the BADC as a check on stability. In this experiment the thresholds are currently set to 50 mV and 200 mV, and typical photomultiplier pulses vary around 1 V.

This unit also provides two other signals to all the DISCOs in its crate, via the CAMAC backplane. The first is the RESET, which is derived from a signal from the logic. The second is the gate for the charge integration which is also started by the leading edge of the RESET and ended by the leading edge of the (delayed) STROBE.

STROBER. This unit provides common-stop timing for all the DISCOs in a crate, as previously described. It has two inputs: a pulse from the 3-FLAVOR MODULE, and the RESET (via the backplane) which is necessary to enable the unit. The pulse from the the 3-FLAVOR starts a gate (STROBE) whose length (65 nsec) is set by the length of a cable. The STROBE is fanned out through 50 Ω cables to enable the circuits of the DISCOs and is also fanned out to the THRESHERs to provide the stop for the charge integration gate. After each STROBE the circuit must be reenabled by the RESET.

BADC. This "Brilliant Analog-to-Digital Converter" is a combined ADC and microcomputer[4] , which reads the contents of the DISCOs via the analog bus.

The ToF system uses the BADC in two modes of operation. In "pass-through" mode the contents of the ADC are transmitted unchanged to the host computer; this is used in calibrating the DISCOs. However in "time-of-flight" mode (used for normal data-taking) it subtracts pedestals, suppresses zero channels [8] and

---

[8]A 'zero channel' is defined in the BADC program as one for which the time at the lower DISCO threshold exceeds a preset value, indicating that no pulse from the photomultiplier passed the threshold.

performs corrections up to second order on the data to convert raw numbers into common units of time and charge, using constants supplied by the on-line calibration. Its action is initiated by the BADC START from the logic, which is produced by the EVENT signal from the trigger[5] or by a psuedo-EVENT signal from the logic during calibration or laser monitoring.

For each photomultiplier that fires, the BADC encodes four pairs of 16-bit words for transmission to the computer. The first word of each pair specifies the photomultiplier number and the type of data. The second word is the value of the datum. The four pairs correspond to the four types of data, namely the times at the low and high threshold, the charge, and the temperature.

BADCs are used throughout the experiment. Such distributed processing reduces the load on the host computer, and minimizes deadtime and subsequent off-line analysis.

SPORT. This "Smart PORT" is the multiplexing interface between the BADC and the crate controllers which sequence the readout of the DISCOs. It also multiplexes the analog busses from the two crates into the BADC. In the second crate, the SPORT is interfaced to the crate controller by the SAM unit.

3.2 LOGIC.

The second section of the system, shown in Fig.11, is NIM switching and control logic. It provides three signals for the CAMAC: the "XING" or time-reference, the RESET, and the BADC START. The control is provided by means of a CAMAC-controlled input-output register (Joerger Enterprises model IR1).

The control levels are labelled CALIB, LASER, and CAL-RESET. The CALIB level enables the system for calibration and disables normal data-taking. Similarly, the LASER level selects laser monitoring and turns on the laser. The CAL-RESET is used in calibration or monitor mode to reenable the circuits after the BADC has been read out.

1) There are three possible time reference signals, multiplexed through coaxial switches to the input of the 3-FLAVOR. These are:

a) The "beam-crossing" signal from SPEAR, used in normal data-taking.

b) The output of a mercury pulser, used in calibration as described later.

c) The inverted output of the vacuum photodiode [9] which samples the laser pulse during monitoring.

2) The RESET level is provided by either one of two gate generators.

a) The gate generator A provides the RESET for calibration and monitoring. This is a continuous level which is set to zero by a time reference signal 120 nsec before the time measurement, and is reestablished after the BADC has been read out, by toggling the CAL-RESET level.

b) The other (B) is used for normal data-taking and produces a pulse of fixed length which is started by the RESET from the trigger logic. This reset occurs every beam-crossing in order to minimize the "memory" effect of the sample-and-hold circuits. This GG is inhibited (blanked) in the calibration or laser monitoring mode of operation. When a candidate event occurs at the lowest level of the trigger logic, the RESET is inhibited until the data have been read or the event has been rejected by a higher level of the trigger logic. Until the next RESET occurs, the STROBERs are disabled and the DISCOs cannot acquire further data.

3) The BADC START initiates the action of the BADC in reading out and processing the contents of the DISCOs. For normal data-taking this occurs several microseconds after the EVENT recorded. For calibration and monitoring it occurs at about the same time as the data-pulses, but there is a substantial internal delay in the BADC which prevents premature readout. The relative timing of this pulse is unimportant, because the BADC START occurs only after the RESET has been inhibited and the DISCOs latch after acquiring data and remain inactive until reset.

---

[9] The photodiode requires positive voltage.

4. On-line Calibration and Monitoring.

The DISCOs are calibrated against a remotely-controllable variable delay containing a set of five RG58 cables, which have nominal values of 2, 4, 8, 16 and 32 nsec. The delays have been measured to a precision of about 75 psec. TTL level inputs to the delay box from the IR1 unit allow 5-bit binary numbers to set delays from 2 nsec to 62 nsec in 2 nsec intervals. The delay cables are switched by using coaxial relays.

4.1 Measuring the Delays of the Calibration Cables

The setup that was used for measuring the cables is shown in Fig.12. A nitrogen discharge tube provided a 4 nsec pulse of light along with a short electrical pulse ($<$500 psec). The electrical pulse was used to start the timing electronics. The light pulse, which was detected by a photomultiplier, provided the stop pulse. The cable whose delay time was to be determined was switched into the start side of the circuit. The pathlength between the light source and photomultiplier was increased by sliding a front-silvered mirror along an optical track until the time interval between start and stop signals was the same as it previously had been. The change in pathlength between the light source and the photomultiplier, divided by the speed of light, gave the delay of the cable.

This arrangement avoided the possible problem of nonlinearity in the timing electronics – only stability was required. In order to eliminate time walk due to variation of pulse height the light was collimated by lenses, and only photomultiplier pulses within 5% of the nominal pulse height were allowed to enable the timing electronics.

4.2 On-line Calibration of the Time-of-flight System

The time-of-flight system is calibrated by the VAX 11/780 that runs the Mark III experiment. The VAX is linked to the CAMAC system by a programmable channel that contains a 16 bit CPU, an interface to the DEC Unibus, and a CAMAC control unit. Communication with non-CAMAC equipment is controlled through a CAMAC-TTL interface module (IR-1).

Precise times are of crucial importance, but charge measurements require only consistency. There is therefore no absolute calibration of the charge scale.

The calibration program begins the calibration by setting the time-of-flight BADC to "pass-through" mode. This allows the DISCO information to be passed to the VAX without any preliminary processing. Signals from a mercury pulser are sent through the calibrated delay cables and distributed to the DISCO inputs by a balanced splitter. The DISCO information is read by the BADC and passed to the VAX. The number of calibration points is controlled by the user, and is currently set to 5 different delays covering 31 nsec, and 5 different pulse heights (at a single delay). The delays and pulse heights are set by the calibration program. The pulse heights are varied by means of a digital-to-analog converter, which controls the high voltage supply for the mercury pulser. The program then calculates the calibration coefficients by a least-squares fit to the data.

Various checks are made to see if the new calibration constants are reasonable. The constants of the channels that are good are stored in the database. The bad channels are flagged. The program loads the newly generated constants into the BADC, using the old values for the bad channels. It then sets the BADC to time-of-flight mode, and goes through the above procedure to generate residuals. The results of the calibration are examined, and if necessary the procedure is repeated. If after several iterations there are persistent bad channels or residuals outside tolerances then it may be necessary to make repairs or to replace the corresponding DISCO.

This calibration affects only the electronics: the off-line calibration is needed to take account of effects in the counters and cables.

4.3 Laser Monitor

At the start of each run and at hourly intervals thereafter during data-taking the normal trigger is disabled and the laser is turned on for approximately 100 pulses. The computer acquires the data in the normal way and writes it to tape in the standard format, but with a distinguishing flag. These data are also analyzed on-line and displayed at the console, in the form of a comparison with a table of

nominal values.

5. Off-line Calibration

5.1 OBJECTIVES.

The purpose of this calibration is to generate constants for use in the analysis to calculate corrected values of times etc. It takes account of all system-dependent effects apart from the electronics (see on-line calibration). Since there are several possible sources of variation the calibration is repeated at approximately daily intervals.

The calibration is concerned with the following effects. First, the transit times of the photomultipliers and the lengths of the cables differ from each other by a few nanoseconds. Secondly there is "time-walk" as the charge of the pulse varies, and the size of this effect varies from counter to counter. And thirdly the measured time depends on where the particle hits the counter. This requires that a measurement be made of the effective speed of light in the scintillator.

5.2 DEFINITIONS AND CONVENTIONS

The MARK III coordinate system is shown in Fig.3 . In what follows Z_c is defined as the value of the z-coordinate of a track extrapolated to the nominal ToF radius of $R_c = 1.18$ m. In certain places it is convenient to use a variable which effectively relates to the distance from one photomultiplier. For this Z_c^s (meaning Z_c with appropriate sign) will be defined as follows. When referring to a photomultiplier at the north end of the detector $Z_c^s = Z_c$, but when referring to the south end the sign is changed and $Z_c^s = -Z_c$. The angle ϕ shown in the figure is the conventional azimuthal angle of right-handed cylindrical polar coordinate systems. The angle θ is the conventional polar angle. The subscripts N and S refer to the north and south ends of the counters.

5.3 PROCEDURE

The time-of-flight for high energy electrons can be determined from the path

length alone. Therefore this calibration is performed with Bhabha [10] events selected independently of the time-of-flight system. These events are used to perform least-squares fits to determine the correction constants described below.

The Bhabha events are selected by the first off-line filter (which rejects junk events and attempts a simple classification of the rest, using only the shower counter, and crude ToF data to reject cosmics). The path length is approximated as a straight line from the vertex. About 4000 to 5000 events, or 8000 to 10000 tracks, are used in each calculation (roughly 180 tracks per counter.) This corresponds to roughly ten runs or one day of data-taking, and is a compromise chosen to have adequate statistics while remaining sensitive to short term drifts.

The filter program supplies values of the coordinates Z_c and ϕ obtained from the barrel shower counter which have been extrapolated to the ToF counters to adequate accuracy, that is about 3 cm in Z and 6 milliradians in ϕ. Both tracks must have associated hits in the ToF counters where they are predicted by the extrapolation. This does not cover quite the whole length of the counter, because the barrel shower counter is not much longer than the scintillators. Particles passing through the very ends of the counters therefore intersect only a part of the barrel and cannot be reliably identified as Bhabhas. Fig.13 shows the mean charge (one counter, both ends) as a function of Z_c. The combined effects of attenuation and angle of incidence are clear.

The effects with which this calibration is concerned are described below in the order of their treatment by the program.

Charge Effects.

The calculation of the optical attenuation length and the mean normalized charge requires only a single pass through the data, and is performed first.

1) If the charges measured at the ends $q_{N(S)}$ are taken as proportional to the number of photons produced then the attenuation length Λ of the counter is

---

[10] In all that follows "Bhabha" is used as a synonym for $e^+e^- \rightarrow e^+e^-$, without distinguishing between the simple QED process and the formation and decay of a ψ.

defined by

$$q_{N(S)} = b_{N(S)} e^{-Z_c^s/\Lambda} \tag{5.1}$$

where $b_{N(S)}$ is a different constant for each photomultiplier. Then for each counter

$$ln(q_N/q_S) = ln(b_N/b_S) - 2Z_c/\Lambda \tag{5.2}$$

Thus Λ is determined for each counter by fitting $\ln(q_N/q_S)$ to a straight line in Z_c. Fig.14 shows this fit for a typical counter. It is found that for some counters there is some nonlinearity at the ends, although the value of Z_c where this sets in varies from counter to counter. Since this effect could distort the results for the rest of the counter length, the fit is performed over the limited range $-1.44 \leq Z_c \leq 1.44$. One obvious explanation of this behaviour is saturation of the ADCs of the DISCOs for the largest pulses. The effect is seen to increase with increasing photomultiplier voltage. Also the effect is greater for Bhabhas than for hadrons which suggests backsplash from electromagnetic showers may enhance the pulse height.

The attenuation lengths Λ of the counters have an average value of 2.5 m and a variance of 0.7 m.

2) The mean normalized charge $q_{0_{N(S)}}$ is found for each counter for Bhabhas. This is calculated from the raw charges $q_{N(S)}$ by dividing out the effects of attenuation and angle to provide a measure of the light produced by a minimum-ionizing particle at normal incidence to the counter. This is used in the off-line analysis, together with the attenuation length, to calculate the energy $Q_{N(S)}$ deposited by a given particle.

$$Q_{N(S)} = Q \frac{q_{N(S)}}{q_{0_{N(S)}}} e^{Z_c^s/\Lambda} \tag{5.3}$$

where Q=10 MeV.

Time Corrections Counter-by-Counter.

— These corrections are calculated individually for each photomultiplier.

3) A different zero-time τ_i is calculated for each photomultiplier i, owing to variation in the lengths of cables, transit times of photomultipliers, etc.

4) The time-to-threshold is a function of pulse height – this is commonly called 'time-walk'. It is well known that this varies over a wide range like

$$t_W = \frac{\alpha}{\sqrt{q}} \tag{5.4}$$

where q is the total charge of the pulse (pC) and α is the coefficient to be measured which is different for each photomultiplier. Fig.15 shows the effect for a typical counter.

The values of α range roughly from 20 to 50 nsec$\sqrt{pC}$, and so the correction may be up to 5 nsec for a pulse of 100 pC.

Global Time Corrections.

The same corrections are applied to all counters, because they contain small higher-order terms, and the limited statistics available for single counters are insufficient for the precision required. Tests confirmed that no significant improvement in resolution was obtained by performing these corrections counter-by-counter.

5) It is found that the time-walk correction of equation (5.4) does not completely describe the variation with charge. A further small correction is needed. This is expressed as a cubic function of the charge.

$$t_q = \sum_{n=1}^{3} D_n q^n \tag{5.5}$$

These corrections are of the order of 100 psec for pulses of 1000 pC [11]

6) The time varies with Z_c as though the effective velocity of light in the scintillator varies slightly along its length. This may be due to variations in pulse shape or to correlations with other correction functions, but at present

---

[11] Typical values of these coefficients are of the order $D_1 \approx 3 \times 10^{-4}, D_2 \approx -3 \times 10^{-7}, D_3 \approx 3 \times 10^{-10}$

there is no obviously acceptable explanation of this behavior. It is corrected with a cubic in Z_c^s.

$$t_V = \sum_{n=1}^{3} C_n (Z_c^s)^n \tag{5.6}$$

This is an empirical parameterization. There is a strong correlation between charge and Z-position, but this has been ignored in the fitting procedure, as no known model gives better resolution.

Typical values of C_1 range from 6.0 to 6.1, while those of C_2 and C_3 are from -0.04 to -0.1. Thus at the ends of the counters the nonlinear corrections are of the order of 100 psec.

The mean effective velocity is $V_{scint} = 16.5$ cm/nsec. This differs significantly from the value quoted (Table 1) for direct transmission in the scintillator (19 cm/nsec), but agrees with other experiments using long counters[6] . A measurement was made of the speed of directly transmitted light in scintillator. It was found that for path lengths greater than about 10 cm the result agreed with that given above for the counters. This indicates that this lower speed is a real effect in the scintillator and not a result of multiple reflections.

Iteration Procedure.

The global and counter-by-counter corrections are calculated by iteration, starting with some set of approximate values. First the global corrections (t_V, t_q) are calculated and subtracted from the measured times. The residuals are accumulated and least-squares-fitted to obtain the counter-by-counter corrections (τ_i, t_W). Next, using the new values, residuals are calculated to refit for the global corrections. The process is repeated several times. The data used in the fits are restricted to points within about 3σ of the expected values, to eliminate the non-Gaussian tails.

Run-by-run Time Corrections.

7) Finally, a global zero-time τ_{run} (averaged over all counters) is calculated. This is the deviation of the mean for each run from the mean for all runs used

in the calibration. This variation is of the order of a few tens of picoseconds per run.

A run usually corresponds to one full tape, i.e. about 2 - 3 hours continuous data-taking or 2 - 3×10^4 events recorded (about 1000 Bhabhas at the $\psi(3.1)$).

The τ_{run} are calculated as mean residuals after all the other calculations are finished. If any large steps were found this would indicate that some substantial change had taken place at that time, and different groupings of runs would give a better calibration. Thus these values are finally always small.

Complete Expresssion for Corrections.

After collecting the five terms, the corrected time for a given photomultiplier is

$$t_{N(S)} = t^{raw}_{N(S)} - \tau_i - \tau_{run} - t_W - t_V - t_q \qquad (5.7)$$

This is now the required expression for the time to be used in the analysis.

5.4 Effects of Different Thresholds

The time correction terms are calculated independently for the upper and lower thresholds. It is expected that the results should be closely correlated, although the form of the relation is not known. Thus the correlations described below are a result of the fit and not imposed *a priori*.

The difference between the times τ_i at the higher and lower thresholds averages about 800 psec with an rms variation of around 250psec.

The time-walk coefficients α are found to have an average of 36 psec$(pC)^{1/2}$ for the lower threshold and 41 for the higher, with a variance of about 6 in each case, that is about $10-15\%$ greater for the 200 mV threshold than for the 50 mV. An early test (on a single counter in an electron beam) covering the range 50 mV to 600 mV showed that α increased linearly up to 400 mV (i.e. a considerable fraction of the total pulse height). Above this voltage, α rose more rapidly, and the resolution, which had been almost constant, also deteriorated sharply.

The value of C_1 is consistently about 1% higher for the higher threshold than

for the lower, and the other two terms compensate in such a way that the final values for both thresholds agree within about 50 psec. There do not appear to be any significant and systematic differences between the two thresholds for the global correction coefficients D_n.

The values of τ_{run} for the two thresholds seldom differ by more than 10 psec, and almost never by more than the mean run-to-run excursions.

6. Data Analysis

6.1 KINEMATICAL INTRODUCTION.

Measurements of the time of flight of particles, taken together with their momentum, provide information on the masses of the particles. In what follows the units of momentum are GeV/c and of mass GeV/c^2.

From kinematics, a given particle type with mass m_i and momentum P has a speed:

$$\beta_i = P/\sqrt{P^2 + m_i^2} \tag{6.1}$$

For a path length L the time-of-flight is:

$$T_i = L/c\beta_i \tag{6.2}$$

For two masses at the same momentum

$$1/\beta_2^2 - 1/\beta_1^2 = (m_2^2 - m_1^2)/P^2 \tag{6.3}$$

Hence the time-difference for the two types is given by

$$\begin{aligned}(T_2 - T_1) &= (L/c)(\frac{m_2^2 - m_1^2}{P^2})(\frac{\beta_1\beta_2}{\beta_1 + \beta_2}) \\ &\leq (L/c)(\frac{m_2^2 - m_1^2}{2P^2})\end{aligned} \tag{6.4}$$

6.2 RESOLUTION OF THE SYSTEM.

Effect of Tracking Errors.

Each track has a kinematically predicted value of the time-of-flight T_I (from equation (6.2)) for the given mass-hypothesis m_I and the measured momentum, with an error that will be found to depend both on m_I and the track parameters. The measured time T is calculated using certain corrections which involve Z_c and are therefore also subject to tracking errors.

Combined Resolution.

Thus the resolution of the system contains, in addition to the intrinsic resolution of the counters, contributions from the track reconstruction. It may be described in terms of the probable error on the difference between the predicted and measured times, or equivalently of the resolution of the mass-squared of the track. This is discussed in detail in appendix A.

6.3 The MARK III Analysis Program.

The analysis of an event is a sequence of operations, each treating one element of the detector separately. First a search is made for all reconstructible tracks in the drift chamber. Next the shower counter data are analyzed and hits are either recognised as continuations of tracks in the drift chamber or else assigned as separate tracks (probably converted photons). Thirdly the ToF data are analyzed, and an attempt is made to associate hits in the ToF with tracks seen in the drift chamber, the shower counter, or both.

The primary object of the time-of-flight section of the analysis is to calculate for each charged track both its mass-squared M^2 (an adequate identifier at low momenta), and the Gaussian probability P_I for each mass-hypothesis m_I. However, several other quantities are also provided which may be useful in physics analysis or studies of the system. The analysis chain is described fully in appendix A.

6.4 Examples of Reconstructed Events.

Three simple events are shown in order to illustrate more graphically the analysis described above.

Fig.16 shows an example of an event containing both charged tracks and

photons converted in the shower counter. This event was kinematically fitted as $\psi \rightarrow \pi^+\pi^-\pi^0$. Figures 17 and 18 show two more clean events fitted to the hypothesis $\psi \rightarrow \gamma\eta'$.

7. Performance of the ToF System

During the Spring of 1983, MARK III collected about 1.5-× 10^6 hadronic events at the J/ψ(3.1). The evaluation of the ToF system presented here is based on subsets of these data, and Bhabhas collected at the same time.

Average resolution. The simplest measure of the time-resolution of the system is provided by the difference between the predicted and measured times (ΔT_I defined in appendix A) for e^+e^- and $\mu^+\mu^-$ events. The Bhabhas were selected by the filter as described earlier, independently of the drift chamber, and the dimuons were selected as charge-balanced two-prong events with an invariant mass between 2.8 and 3.2 GeV and with each track having an associated hit in the muon counter. This is shown in Figs.19 and 20 in which the distributions are fitted with a Gaussian. The fitted widths are $\sigma = 171$ and 175 psec respectively.

The resolution as measured using hadrons is complicated by the much larger variation in β and curvature of the path, and the errors on these which have been described in a previous section. Fig.21 shows a resolution of 189 psec measured for pions from events kinematically fitted (5C) to the hypothesis $\pi\rho$. The resolution is significantly larger than for Bhabhas and the non-Gaussian tail is considerably bigger on the positive side.

M^2 and β vs P. Figures 22, 23, and 24show scatter plots of β and M^2 *vs* momentum for tracks with T_{qual}=1 from hadronic events[12] . The π and K are visibly separated up to 0.9 GeV/c, while protons are separated at all momenta. At the 2σ level, pions and kaons are separated up to 1.2 GeV/c.

Laser Results. A single counter was found to have a time dispersion of about

---

[12] T_{qual} is defined in Appendix A. $T_{qual} = 1$ means the cleanest data.

110 psec for each end separately, with charges about 35% greater than the mean for Bhabhas. The data were cut in a narrow range of charge, and no corrections for time-walk were applied. As shown in Fig.11 the only essential difference in the electronics for the laser test is that the time-reference is taken from the photodiode in place of the beam pickup. It is not possible at present to account quantitatively for such low values of resolution, although it suggests that errors other than those from photoelectron statistics may be larger than expected, and possibly reducible. Then the laser values might represent a lower attainable limit of resolution.

ACKNOWLEDGEMENTS

Thanks are due to R. Mozley, J. Rothberg, D. Dorfan and B. Sukiennicki for assistance during the design stages of the system, to H. Guldenmann and the staff of the machine shop of the University of Washington's Physics Department for fabrication of the light guides, to D. Forbush for assembling and testing the counters and other assistance during the project, to D. Hutchinson, G. Mazaheri, F. Toevs and J. Bernstein for assistance with the electronics, to Knut Skarpaas, Bob Eisele and John Grant for help in installing the counters, to Brian Swanson and Fred Motteler for assistance with various stages of the project, to D. Hitlin for providing the discs that join the photomultipliers to the light guides, and to A. Odian and F. Villa for valuable discussions. We are grateful to the SLAC Illustrations Department for their skill and patience in preparing the figures for this paper.

We thank the NSF for support under grants PHY-802-2207 and PHY-811-2208.

APPENDIX A

Tracking errors.

The drift chamber code describes the reconstructed tracks in terms of five parameters t_j, of which the following three contribute to the time errors: $t_1 =$

κ (P_{tr}^{-1}, component of momentum transverse to beam), t_2 =s ($\cot\theta$, the polar angle), and $t_3 = Z_b$ (Z at point of nearest approach to the beam axis). For each track it also supplies an error-matrix S^{jk} which is a function of these quantities.

In order to calculate the error on T_I it is necessary to define derivatives of the time with respect to the track variables t_j, by

$$a_j = \frac{\partial T_I}{\partial t_j} \qquad (A.1)$$

Then the error on the predicted time is:

$$\sigma_{T_I}^2 = \sum_{j=1}^{3}\sum_{k=1}^{3} a_j a_k S^{jk} \qquad (A.2)$$

The elements of the error matrix vary in a limited range for most tracks, and the following example is typical. These are means with variances of similar magnitude. The $\pm$ symbols indicate that these mean values change sign with the charge of the track.

Typical Error Matrix S^{jk}

	1	2	3
1	0.0015	$\mp 8 \times 10^{-5}$	$\pm 5 \times 10^{-5}$
2		2×10^{-4}	-1×10^{-4}
3			2.5×10^{-5}

The coefficients a_j (equation (A .1)) have the explicit form:

$$a_1 = \frac{\partial T_I}{\partial \kappa} = \left(\frac{\tan(\varphi)}{\varphi} - \beta_I^2\right)\frac{T_I}{\kappa} \qquad (A.3)$$

where φ is the angular difference between the tangents to the tracks at its ends (in radial projection, calculated from the measured P_{tr}), and β_I is calculated from the measured momentum and the hypothesis m_I as in equation (6.1) . Two terms are present because variations in κ change both the path length and the momentum (and hence the speed) of the particle.

$$a_2 = \frac{\partial T_I}{\partial s} = T_I \beta_I^2 \sin(2\theta)/2 \qquad (A.4)$$

Variations in s also produce corresponding changes in both the path length and the momentum of the particle, but the expression simplifies to a single term.

$$a_3 = \frac{\partial T_I}{\partial Z_b} \equiv 0 \qquad (A.5)$$

The reason for including this term will be made clear below.

Fig.25 shows the variation of a_1 and a_2 in the plane of P_z and P_{tr} as contours in the range $45° \leq \theta \leq 90°$. The values of a_1 are symmetrical about 90° while the values of a_2 change sign, owing to the $\sin(2\theta)$ term.

Time-of-Flight Analysis.

The time-of-flight section of the analysis code is designed to fill an array for each track. The inputs needed for this calculation are the raw ToF data and information from the drift chamber or the shower counter (which includes the coordinates (Z_c, ϕ) of the extrapolated intersection with the time-of-flight counters, the integrated path length (L), the track parameters t_j, and the error matrix S^{jk}.)

The basic purpose of the ToF system is to identify charged tracks measured in the drift chamber. However photons that pass through a counter that has registered a charged track may affect the measurement and cannot be ignored in the analysis. A study of isolated photons showed that roughly half of the photons that are detected in the shower counter have associated hits in a ToF counter. These may be due to conversion in or before the ToF counters, to Compton scattering in the counter, or to "backsplash" from photons converting in the first couple of layers of the shower counter. There is also a problem with random coincidences, when part of a shower is misidentified as a separate photon, and this is aligned with a counter that is hit by a charged track.

Matching Counters with Tracks.

For each track, a search is made for an associated counter. The program prepares lists of tracks and hit counters, then examines all combinations independently. The course of the subsequent analysis is affected by the number of tracks associated with a given counter, as discussed later.

There are three possibilities. First, and of most interest, a drift chamber track projects into the time-of-flight counters. The track is extrapolated to a radius of 1.18 m, roughly in the middle of the counter, and the angle ϕ is calculated for this point. This is used to predict the counter that will be hit. If a counter is found to be hit within one counter width on either side of the predicted position (searching first for counters with signals in both photomultipliers) then it is associated with the track. The accuracy of the extrapolation is generally much better than is implied by this loose criterion. This is shown in the histogram (Fig.26) of the difference (DCT) between the predicted and the actual counter hit.

Secondly, a photon (track seen only in the shower counter), may have associated hits in the time-of-flight. In this case the ϕ angle of the shower counter track is used to predict the counter hit. The same method as above is used to associate counters with tracks.

Thirdly, a counter may have a hit without being associated with any track in the drift chamber or shower counter. Some of these hits are due to tracks which traverse the edges of two counters; however only one of the two counters involved will be treated as associated with the track and the other will have no association. (Although only one counter can be associated with a given track, a given counter can be associated with more than one track.) Other cases involve delta-rays or interactions in an adjacent counter, and in still others the hit counter is truly isolated without any nearby tracks. These unassociated hits are recorded with the rest.

Charge Sharing between Tracks.

If two well-separated drift chamber tracks [13] hit the same counter, their times are calculated from the time at the photomultiplier nearest to each of them. Then the total charge at each photomultiplier is recalculated to include only that deposited by the first of the two pulses, q_{NN} and q_{SS}. It is assumed that the pulses are far enough apart that they can be treated as independent

---

[13] These are defined as those more than 30cm apart, which corresponds to about 2 nsec difference in the scintillator.

for the calculation of the time-walk correction. There are two unknowns (the number of photons produced by each track) and two measured quantities (the charges in each photomultiplier q_N and q_S) related by two equations which state that the measured charges are the sums of the photons produced reduced by the attenuation appropriate to the particular counter and the distance. These equations are solved to give the energy in each pulse. The value of the flag T_{qual} (see below) indicates that the ToF for that track is derived from only one photomultiplier. If Λ is the attenuation length of the counter and $S = (Z_N + Z_S)/\Lambda$ and $D = (Z_N - Z_S)/\Lambda$ then

$$\begin{aligned} q_{NN} &= (q_N e^{-D} - q_S e^{-S})/(e^{-D} - e^{D}) \\ q_{SS} &= (q_S e^{-D} - q_N e^{S})/(e^{-D} - e^{D}) \end{aligned} \tag{A.6}$$

Calculation of the Time-of-flight.

For each counter hit the associated time-of-flight T and the corresponding speed β are calculated. The time T is normally calculated as a weighted average of the corrected times at the two ends of the counter:

$$T = (t_N w_N + t_S w_S)/(w_N + w_S) \tag{A.7}$$

where

$$w_{N(S)} = 1/\sigma^2_{N(S)} \tag{A.8}$$

and the corrected time $t_{N(S)}$ for each end is given by equation (5.7) (using charge-sharing where necessary for the time-walk). The intrinsic resolutions of the counters σ_N and σ_S were determined empirically (using Bhabhas) as quadratic functions of Z_c, and are shown in Fig.27.

When only one of the two photomultipliers fired, then

$$T = t_{N(S)} \tag{A.9}$$

The upper threshold is used except when the pulse height is too small [14] and the lower threshold value is then used. No algorithm has yet been devised

[14] At present a pulse is considered too small if the time at the upper threshold exceeds 45 nsec because this corresponds to the overflow channel of of the

which, using both thresholds together, gives an improvement in resolution for particle data, although laser tests suggest this may eventually be feasible.

The measured β of the track is found from the time T and the path length L determined by the drift chamber. This is used in calculating the mass-squared of the track.

Errors on the Time-of-Flight.

The errors on T have two sources. First in importance is the intrinsic resolution $\sigma_{N(S)}$ of the counters (in which is included the variation of the time-reference, although this is of a different physical origin [15]) Second is the error from extrapolation previously described.

The effect of errors in Z_c on the calculated time T are expressed by $\frac{dT}{dZ_c}$ (or $\frac{dT}{dZ_c^s}$) which (from equation (A .7)) normally has the form

$$\frac{dT}{dZ_c} = (\Delta - (w_N - w_S)/V_{scint})/(w_N + w_S) \qquad (A.10)$$

where the speed has been treated as constant and

$$\Delta = -T(\frac{dw_N}{dZ_c} + \frac{dw_S}{dZ_c}) + t_N \frac{dw_N}{dZ_c} + t_S \frac{dw_S}{dZ_c} \qquad (A.11)$$

When only one photomultiplier is used it has the simpler form

$$\frac{dT}{dZ_c^s} = V_{scint}^{-1} \qquad (A.12)$$

The dominant term in equation (A .10) is that in V_{scint} (which comes directly from the z-correction) whereas Δ (from the derivatives of the weights) is almost negligible. When $t_N = t_S = T$, the value of the expression in equation (A .10) is a function of Z_c only and is nearly linear with slope 1.6 nsec/m. However, if

---

DISCO (the pulse never reached that threshold). This is very rare for charged particles.

[15] This has been estimated at about 70 psec, but there are considerable uncertainties. The method of determining the intrinsic resolution of the counters did not eliminate this effect.

the two times differ by a nanosecond, this only affects Δ and the value changes by only 2 psec/cm at $Z_c = 1.5$ m.

The Z_c-dependent errors can be treated like those already discussed under tracking errors. The coefficients b_j are defined by analogy to the a_j, as derivatives with the track parameters $\frac{\partial T}{\partial t_j}$. Obviously, by definition: $b_1 = \frac{\partial T}{\partial \kappa} \equiv 0$. The b_2 and b_3 terms contain the effect of errors in Z_c on the the measured ToF.

$$b_2 = \frac{\partial T}{\partial s} = R_c \frac{dT}{dZ_c} \qquad (A.13)$$

where $\frac{dT}{dZ_c}$ was defined by equation (A .10) or (A .12) , and R_c is the nominal ToF radius (1.18 m). The term b_3 just represents the effect of the uncertainty in the starting point (and therefore the end point Z_c) of the track.

$$b_3 = \frac{\partial T}{\partial Z_b} = \frac{dT}{dZ_c} \qquad (A.14)$$

Time Resolution of System.

Each track has a measured time T, and a kinematically predicted value T_I (from equation (6.2)) for the given mass-hypothesis m_I and measured momentum. The difference ΔT_I is calculated, with its probable error σ_I, which contains uncorrelated terms from the scintillator and from the tracking in the drift chamber:

$$\Delta T_I = T - T_I \qquad (A.15)$$

$$\sigma_I^2 = \sigma_{scint}^2 + \sigma_{dc}^2 \qquad (A.16)$$

The intrinsic resolution of the scintillator is given by

$$1/\sigma_{scint}^2 = 1/\sigma_N^2 + 1/\sigma_S^2 \qquad (A.17)$$

and is shown as a function of Z_c in Fig.27.

The contribution to the resolution from the tracking in the drift chamber, σ_{dc}, includes effects on both T_I and T, and therefore involves the coefficients a_j and b_j which have been defined previously. Let:

$$c_j = \frac{\partial \Delta T_I}{\partial t_j} = b_j - a_j \qquad (A.18)$$

Then:

$$\sigma_{dc}^2 = \sum_{j=1}^{3} \sum_{k=1}^{3} c_j c_k S^{jk} \qquad (A.19)$$

Mass-Squared of Track .

The mass-squared is calculated from the momentum P and the measured β.

$$M^2 = P^2(1-\beta^2)/\beta^2 \qquad (A.20)$$

This is normally distributed around the true value with a σ that can be shown to be directly proportional to the time resolution of the system as defined in equation (A .16) ,

$$\sigma_{M^2} = \frac{2EP}{t_0}\sigma_I \qquad (A.21)$$

where $t_0 = \beta T = L/c$ — from equation (6.2) [16] .

Thus at low momenta the mass resolution is much less than the mass differences, and it is possible to use a simple mass cut to determine the identity of a particle. However, the σ_{M^2} varies approximately as P^2, so that at higher momenta the probabilities P_I, described below, must be used.

Probability of Mass Hypotheses.

At higher momenta, more than one mass-assignment for a track may be compatible with the measured time T and the errors of measurement. Therefore,

---

[16] From geometry $4.0 \leq t_0 \leq 5.6$, with a mean value of 4.6 nsec, assuming isotropy.

for each possible mass hypothesis m_I (π , K, P, e), the program calculates the probability P_I that the measured time should be T, given the values of the track parameters. This is calculated from the difference ΔT_I and its error σ_I according to:

$$P_I = e^{-(\Delta T_I/\sigma_I)^2/2} \qquad (A.22)$$

Energy Deposited in Scintillator.

An estimate of the energy E_{tof} deposited in the ToF counter is calculated as the mean of values derived from the two photomultipliers: $E_{tof} = (Q_N + Q_S)/2$. The $Q_{N(S)}$ is calculated from equation (5.3) , using the measured charge $q_{N(S)}$ (or $q_{NN(SS)}$ if the charge has been shared according to equation (A .6)). As an example, using pions, Fig.28 shows how the mean E_{tof} varies with Z.

Z measured by ToF alone.

As a consistency check, the Z-value of the hit is calculated from the ToF data alone (Z_{tof}). This is used with other information to assign a flag T_{qual} to the track that may be used in later decision making.

The values of times t_{N_0} and t_{S_0} for the two ends are calculated including all the corrections described previously except those for Z_c. The corrections are such that for tracks at $Z_c = 0$ the times from the two ends are equal. Thus the difference of times from the two ends $\Delta T_{ends} = t_{N_0} - t_{S_0}$ is a measure of the distance from the middle:

$$Z_{tof} = \frac{\Delta T_{ends}}{2} V_{scint} \qquad (A.23)$$

Fig.29 shows the difference $Z_{tof} - Z_c$ which has a peak at zero corresponding to well measured drift chamber and ToF data. Tests have shown that it is adequate for this measurement to use only the linear term (V_{scint}) and ignore the higher order coefficients that are needed for the full time correction (equation (5.6)).

Quality Flag for ToF Measurement.

The flag T_{qual} describes the measurement, with implications regarding quality. This is to be used in subsequent physics analysis. The values of T_{qual} are described below (these are simply flags - the numerical values have no significance). The percentages in brackets refer to a typical sample of charged tracks at the ψ. These are from unselected data, but the distribution depends strongly on the numbers of charged tracks and gammas.

0 Single track hits a counter, but with poor z-agreement, $|Z_{dc} - Z_{tof}| > 0.1\ m$. The time resolution is poor, with wide tails. [9.4%]

1 Ideal case when a single track hits a counter and the time difference of the ends gives a position Z_{tof} in agreement with that from the drift chamber: $|Z_{dc} - Z_{tof}| \leq 0.1\ m$ This ascribes the greatest reliability to the ToF information. [67.1%].

2 In this case two tracks hit the counter and are well separated in z. The charge is shared between them as described previously. The time is measured from the photomultiplier nearest the track. [6.8%].

3 The track appeared to extrapolate to the ToF counters but no hit was recorded. These tracks are usually at the lower limit of momentum (around 80 MeV/c) or near the ends of the counters. They are almost entirely due to the loose cuts used on the extrapolation or to tracking errors in Z. [5.8%].

6 In this case a ToF counter recorded hits at both ends, but was not associated with any other track.

16 In this case a ToF counter recorded a hit at only one end, and was not associated with any other track.

7 This indicates uncertainty about z. Either two tracks extrapolate to the counter and one (or both) has poor z-value, or else more than two tracks hit the counter. All tracks have the same T_{qual}. [7.1%].

8 In this case one or more tracks hit the counter but only one of the pho-

tomultipliers registered a hit. [2.4%].

9 In this case there are two tracks, and the value of Z_{tof} agrees with Z_{dc} for one of them, which is given $T_{qual} = 2$. The time measured for the other is then presumed to be only a lower limit, and is indicated by $T_{qual} = 9$. [1.4%].

REFERENCES

1. SLAC-PUB-3222 D. Bernstein et al, The Mark III Spectrometer; SLAC-PUB-3140 W.Toki et al, The Barrel Shower Counter for the MARK III Detector at Spear.
2. J.E. Grund, SLAC-PUB 2416 (Oct 1979)
3. PEP-NOTE-329 J-L Pellegrin. This unit was designed for use in the PEP storage ring. It is gated by the r.f. signals, and '3-Flavor' refers to the fact that, since PEP has three bunches and six interaction regions, each detector must select the appropriate phase relationship between them in order to measure time relative to the correct bunch. This feature is not used at SPEAR.
4. M. Breidenbach et al, SLAC-PUB 2032 (Oct. 1977) and IEEE Tran. Nucl. Sci. NS-25 no.1 (1978) 706-710.
5. IEEE Transactions on Nuclear Science, Vol.NS-30, p.236 J. J. Thaler at al.
6. For example NIM **134** (1976) 261, W. Braunschweig et al.

FIGURE CAPTIONS

1. Transverse cross-section of the MARK III detector.
2. Axial cross-section of the MARK III detector.
3. Time-of-Flight counters assembled on the drift chamber, with detail showing the mounting strap and pressure pad.
4. An assembled counter, with dimensions in centimeters.
5. Circuit of the photomultiplier base.
6. Prism and steel conduit assembly for fibers. The prism was made in two parts in order to have a polished surface at the end of the hole for the fiber.
7. Ferrule for the end of an optical fiber. The fibers have an inner quartz core which is in contact with the ferrule directly only at the very end.
8. Diffusor box assembly for laser and fibers. The box is one foot long. The number and position of the diffusing quartz plates can be varied. The 'Matrix' is the closely packed hexagonal array of fiber ends.
9. Block diagram of ToF Analog Electronics. Each crate contains twelve DISCOs, a THRESHER and a STROBER. In addition, one crate has a BADC and a SPORT module. The MUX and the 3-Flavor module are in a NIM crate.
10. Response of DISCO to photomultiplier pulses with varying attenuation.
11. Block diagram of ToF Control Electronics. (a) In normal data-taking both the levels CALIB and LASER are logical 0. Then the RESET is taken from the trigger logic via gate generator B. In this case it is a fixed length and stops 120 nsec before each XING pulse. The BADC START comes from the trigger logic via AND gate D. (b) In calibration or monitor mode, either the CALIB or LASER level is logical 1. Then, if both the CAL-RESET level and the RESET from gate generator A are logical 0, the BADC START is the time-reference pulse gated through AND gate C. Another output of C starts the gate from A, which then inhibits C. The gate is stopped by the leading edge of the next CAL-

RESET pulse, when the data have been read out. The inverted output of A is used for the RESET, and B is blanked off. Since the inverted output is used, the RESET level is started by the CAL-RESET pulse, and stopped by the pulse from C 120 nsec before the XING.

12. Test Setup for Calibrating Delay Cables.

13. a) Charge distribution in a single counter. b) and c) Mean charge versus Z_c for Bhabhas separately for both ends. The shape is due to a combination of attenuation (exponential drop) and the path traversed in scintillator ($1/\cos\theta$).

14. Fitted attenuation length of a counter, showing the deviation from linearity at the ends.

15. Time walk for a single photomultiplier showing deviations from linearity at low pulse height.

16. Reconstructed $\pi^+\pi^-\pi^0$ event. The π^+ deposited E_{tof}=9 MeV and the π^- 11 MeV in the scintillator. Both times agree with the pion hypothesis, and the values of Z_{tof} agree well with the drift chamber extrapolation (T_{qual}=1). Only one of the two photons from the π^0, which converted in layer 3 of the shower counter, is associated with a ToF counter. It deposited less than 1 MeV in the counter and the pulse heights were so low that only the lower thresholds were triggered. So this photon probably Compton scattered in the scintillator.

17. Reconstructed $\psi \rightarrow \gamma\eta'$ event. The π^- track passed close to the edge of the counter, but deposited 13 MeV, has T_{qual}=1, and has M^2=0.099 GeV^2. Owing to the high momentum it has non-zero probabilities for both pion and kaon hypotheses. However, the pion is twice as probable as the kaon. The π^+ track clipped the edges of two counters, and deposited 2 MeV in the one associated with the track, having T_{qual}=1 and M^2=0.007 GeV^2. Owing to the low momentum, only the pion probability is non-zero. The track deposited 1 MeV in the adjacent counter and has Z_{tof} consistent with the track extrapolation. Thus, both tracks are clearly identified pions. Neither converted photon has

an associated hit in the counters.

18. Fitted $\psi \rightarrow \gamma\eta'$ event. Both tracks pass through a single counter, 1.49 m apart in Z, and have T_{qual}=2. The time for each track thus comes from a single photomultiplier, and the charge is shared in the manner described. The π^- track deposits 11 MeV and has M^2=-0.117 GeV^2; the π^+ deposits 10 MeV, with M^2=0.026 GeV^2. Both tracks satisfy the pion hypothesis.

19. Time dispersion ΔT_I from Bhabhas. The tails are seen to be non-Gaussian, and the fit is performed for the range -400 to 400 psec.

20. Time dispersion ΔT_I from dimuon events. The resolution is obtained by fitting to a Gaussian in the range -400 to 400 psec.

21. Time dispersion ΔT_I for pions from $\psi \rightarrow \pi\rho$. The resolution is obtained by fitting to a Gaussian in the range -400 to 400 psec.

22. Scatter plot of mass-squared versus momentum for hadronic events.

23. Mass-squared at low momentum showing pion-electron separation and a small muon signal between them.

24. Hadronic data displayed as β vs P.

25. Contour plots of the coefficients a_1 and a_2 in P_z and P_{tr} for pions, kaons and protons, showing the rapid increase with mass for a_1. The units of a_1 are nanoseconds per GeV/c and of a_2, nanoseconds.

26. Extrapolation accuracy in azimuth from drift chamber to ToF, expressed as the distance DCT across the width of the counter, measured from the center. The error is of the order of a few % of a counter width. The data used were kinematically fitted $\pi^+\pi^-\pi^0$ to reduce the probability of using events with errors in track reconstruction by the drift chamber code. The mean energy deposited in the counter (E_{tof}, described later) is plotted against ADCT (the distance from the middle of the counter), and shows a drop at the edge for particles which did not traverse the whole thickness of scintillator, followed by a rise (with large errors because of small statistics) when the adjacent counter was hit.

27. Intrinsic time resolution function used for all counters. The resolutions

for the two ends are mirror images of each other (being functions of Z_c^s).

28. The mean E_{tof} *vs* Z_c (for pions from the reaction $\bar{\pi}^+\pi^-\pi^0$) shows the variation of the path length in the scintillator as the angle of incidence increases.

29. Histogram of z-difference (DZ) from ToF and drift chamber. This quantity is cut at 10 cm for T_{qual}=1.

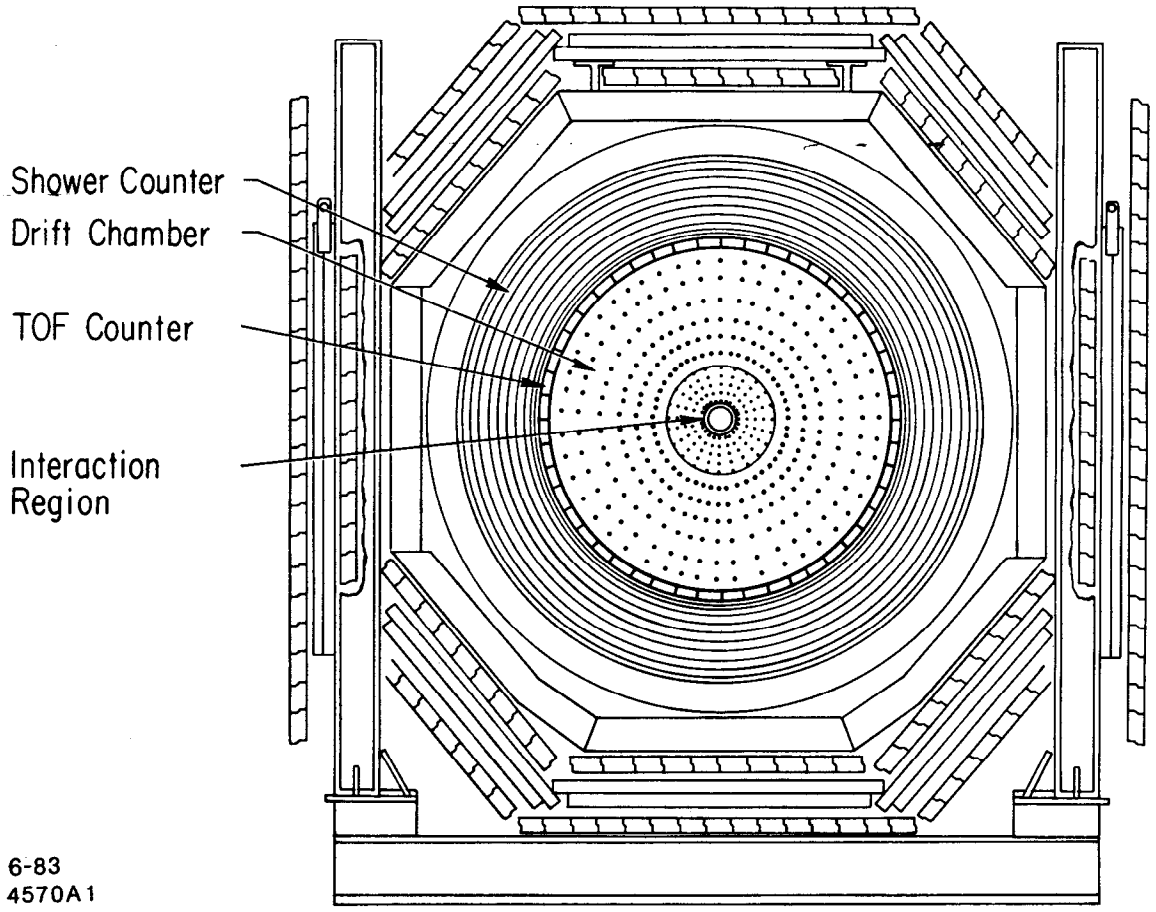
Shower Counter
Drift Chamber
TOF Counter
Interaction Region
6-83
4570A1

Fig. 1

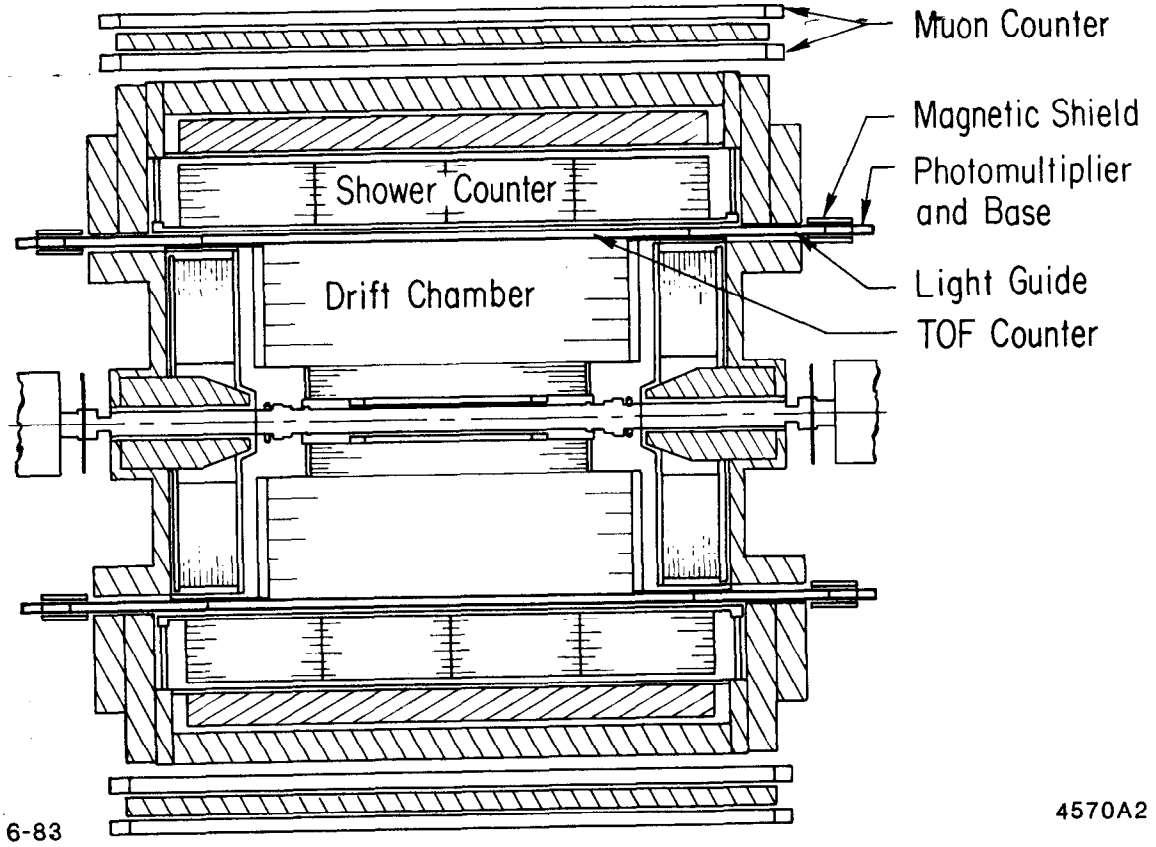
Muon Counter
Magnetic Shield
Photomultiplier and Base
Shower Counter
Drift Chamber
Light Guide
TOF Counter
6-83
4570A2

Fig. 2

MARK III TOF

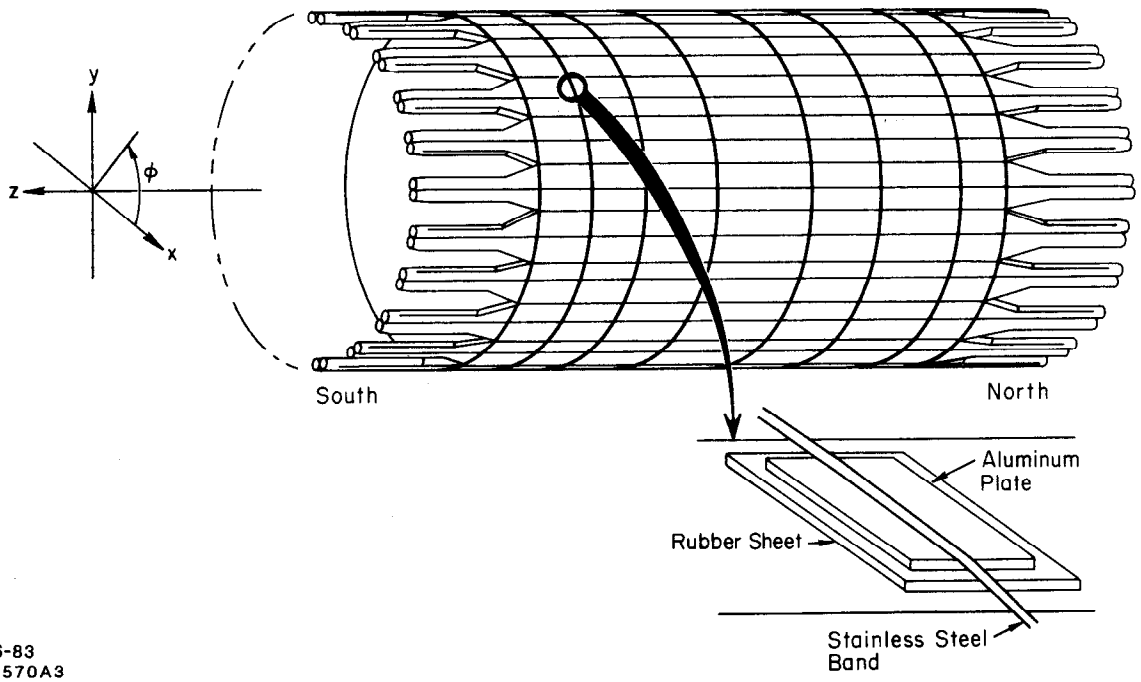

6-83
4570A3

Fig. 3

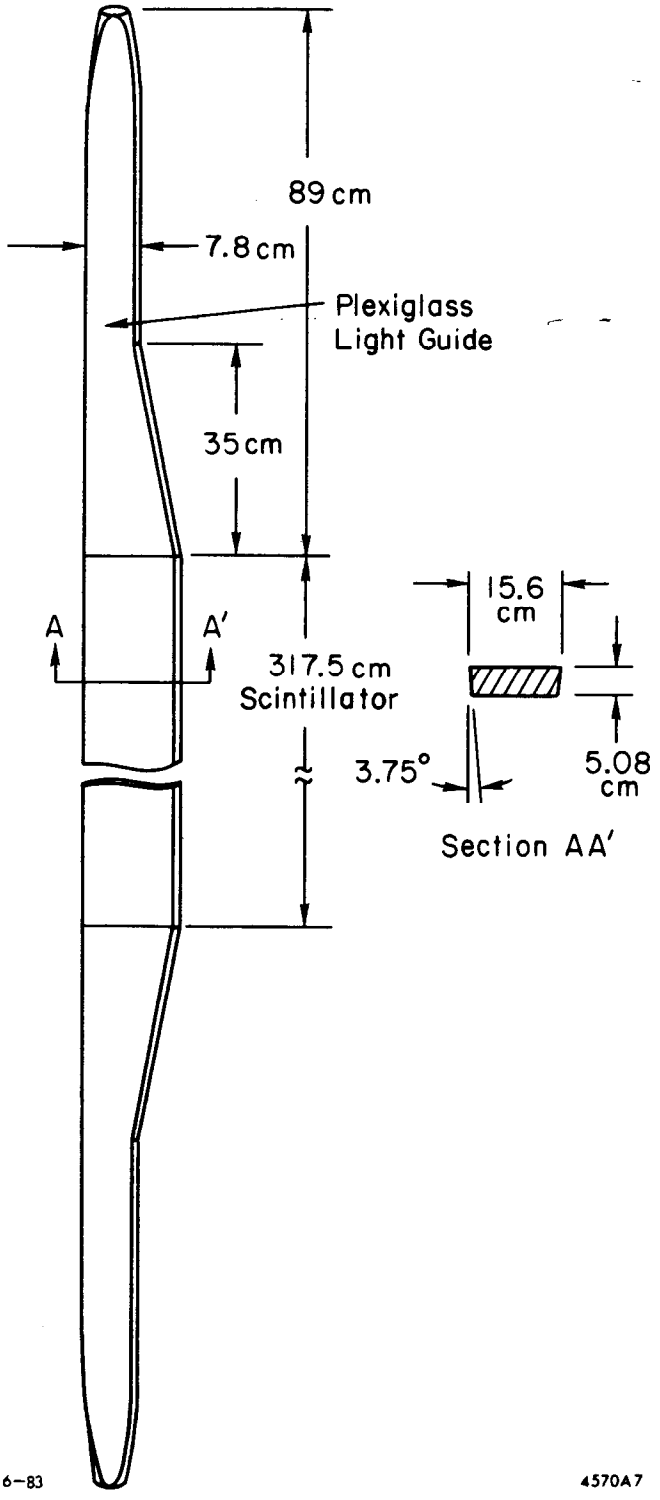
89 cm
7.8 cm
Plexiglass
Light Guide
35 cm
A
A'
317.5 cm
Scintillator
15.6
cm
3.75°
5.08
cm
Section AA'
6-83
4570A7

Fig. 4

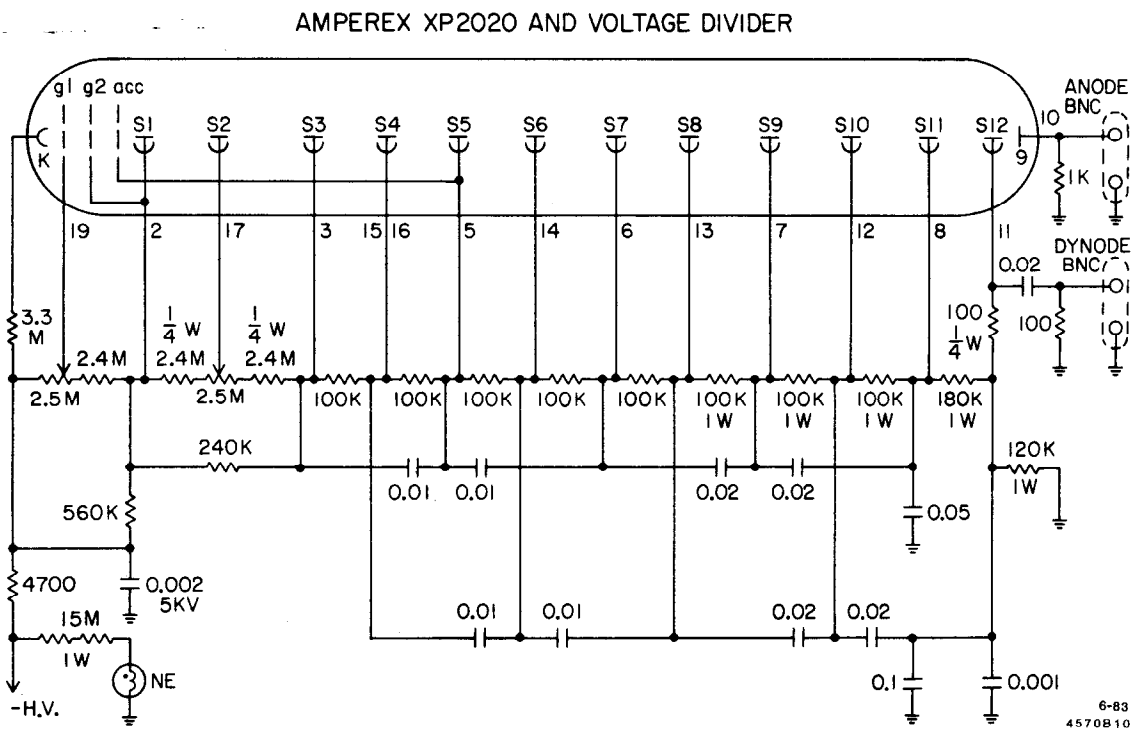
AMPEREX XP2020 AND VOLTAGE DIVIDER
g1 g2 acc
K
S1 S2 S3 S4 S5 S6 S7 S8 S9 S10 S11 S12
ANODE BNC
10
9
1K
19 2 17 3 15 16 5 14 6 13 7 12 8 11
DYNODE BNC
0.02
3.3 M
1/4 W
1/4 W
2.4M 2.4M 2.4M
100
1/4 W
100
2.5M 2.5M
100K 100K 100K 100K 100K 100K 1W 100K 1W 100K 1W 180K 1W
240K
120K 1W
0.01 0.01 0.02 0.02
0.05
560K
4700
0.002 5KV
15M 1W
NE
-H.V.
0.01 0.01 0.02 0.02
0.1
0.001
6-83
4570B10

Fig. 5

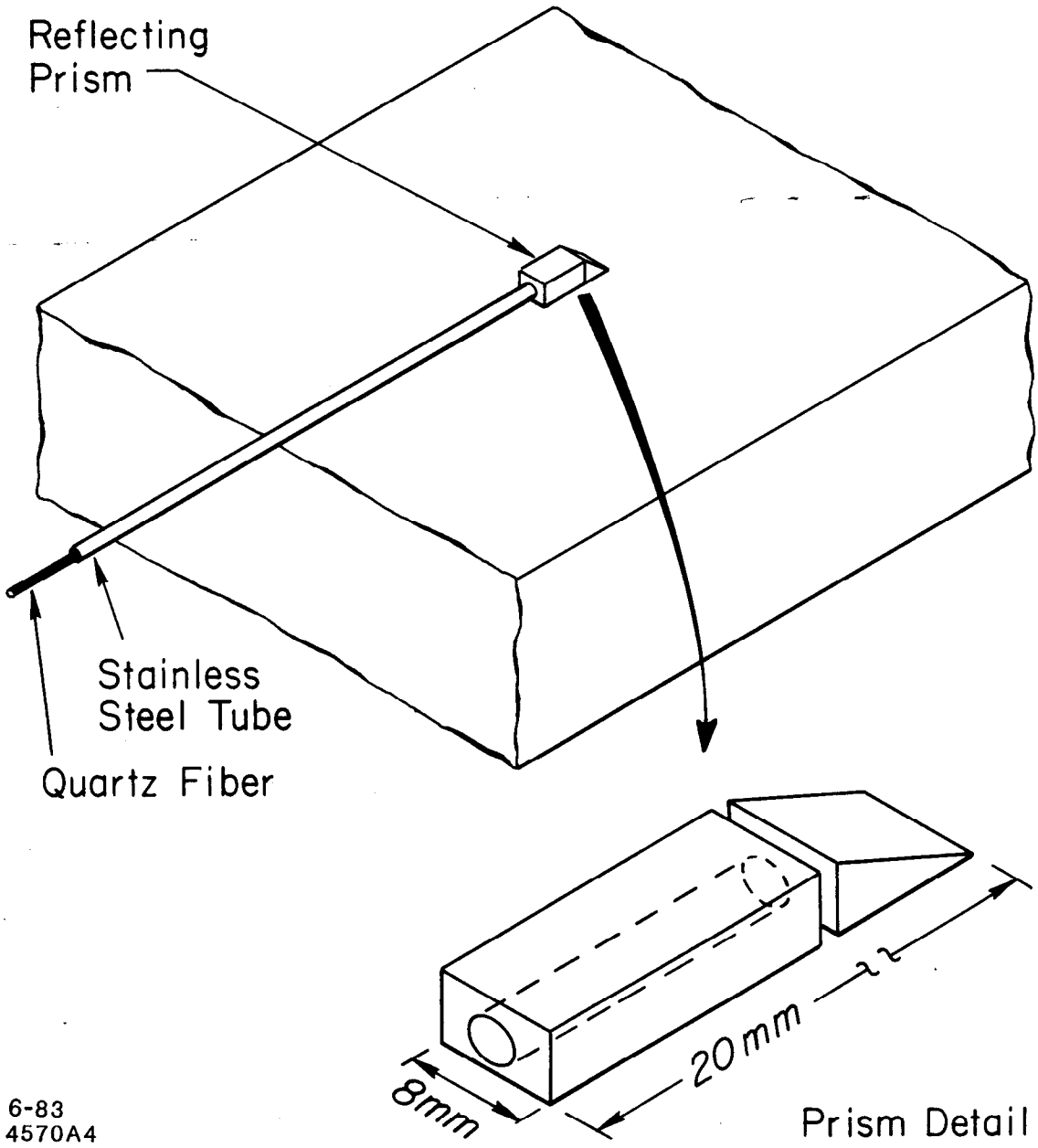
Reflecting
Prism
Stainless
Steel Tube
Quartz Fiber
8mm
20mm
Prism Detail
6-83
4570A4

Fig. 6

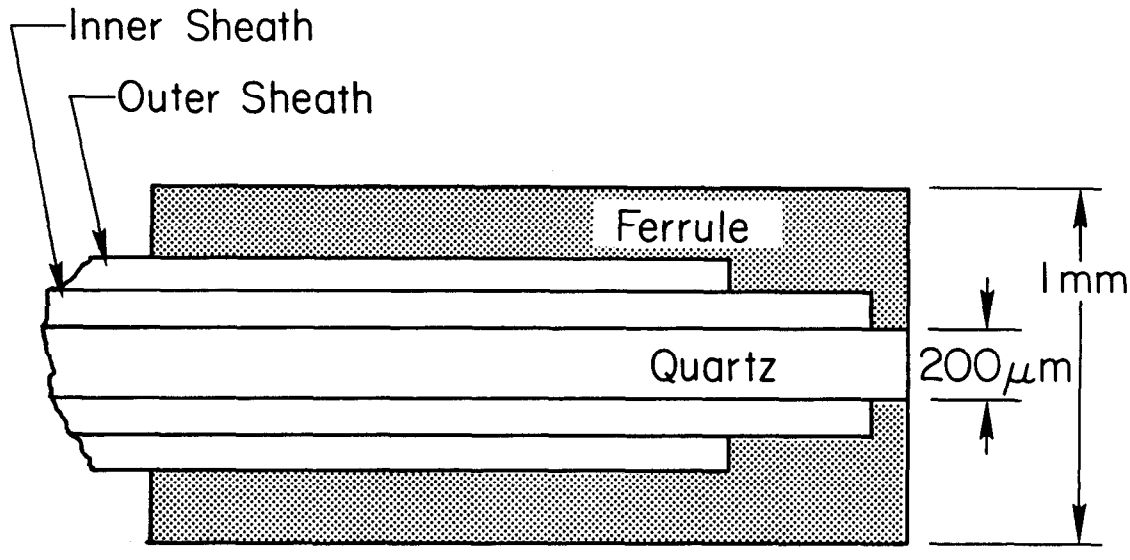

7-83

Quartz Fiber With Ferrule

4570A21

Fig. 7

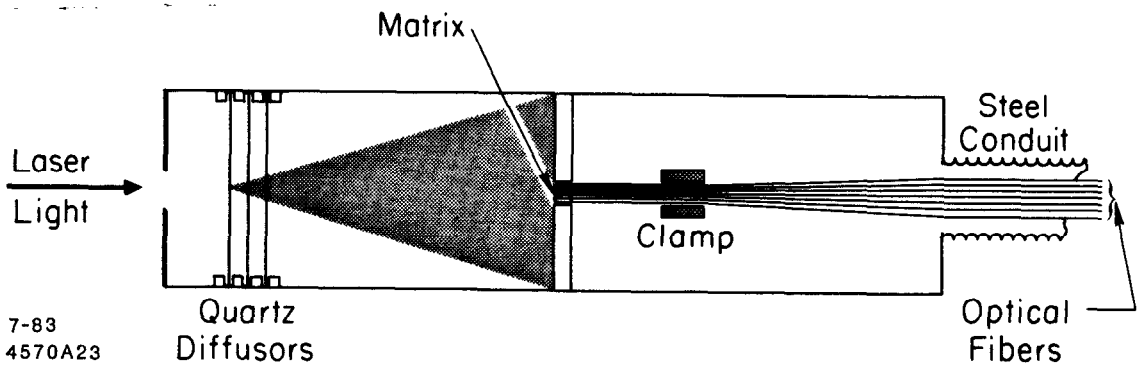
Matrix
Steel
Conduit
Laser
Light
Clamp
Quartz
Diffusors
Optical
Fibers
7-83
4570A23

Fig. 8

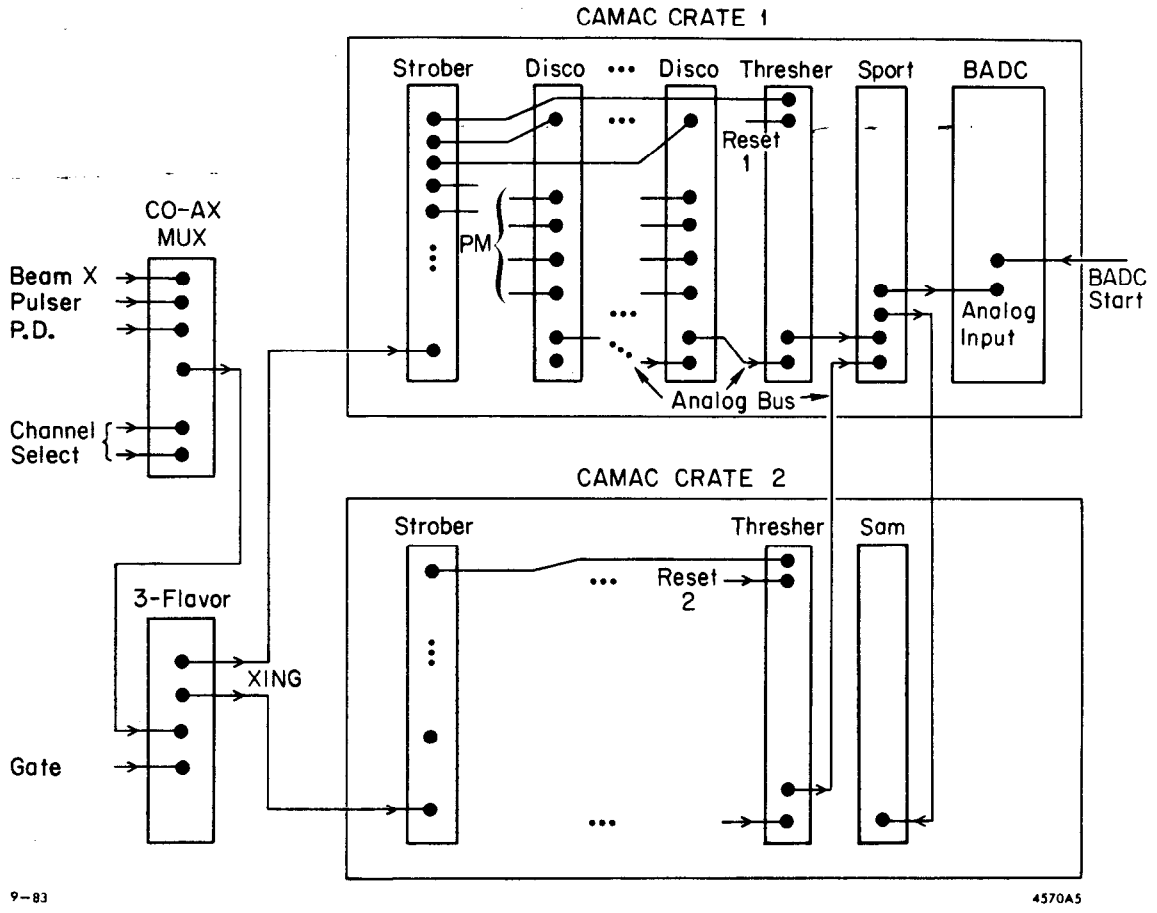
CAMAC CRATE 1
Strober
Disco
Disco
Thresher
Sport
BADC
Reset 1
PM
CO-AX MUX
Beam X
Pulser
P.D.
Channel Select
BADC Start
Analog Input
Analog Bus
CAMAC CRATE 2
Strober
Thresher
Sam
Reset 2
3-Flavor
XING
Gate
9-83
4570A5

Fig. 9

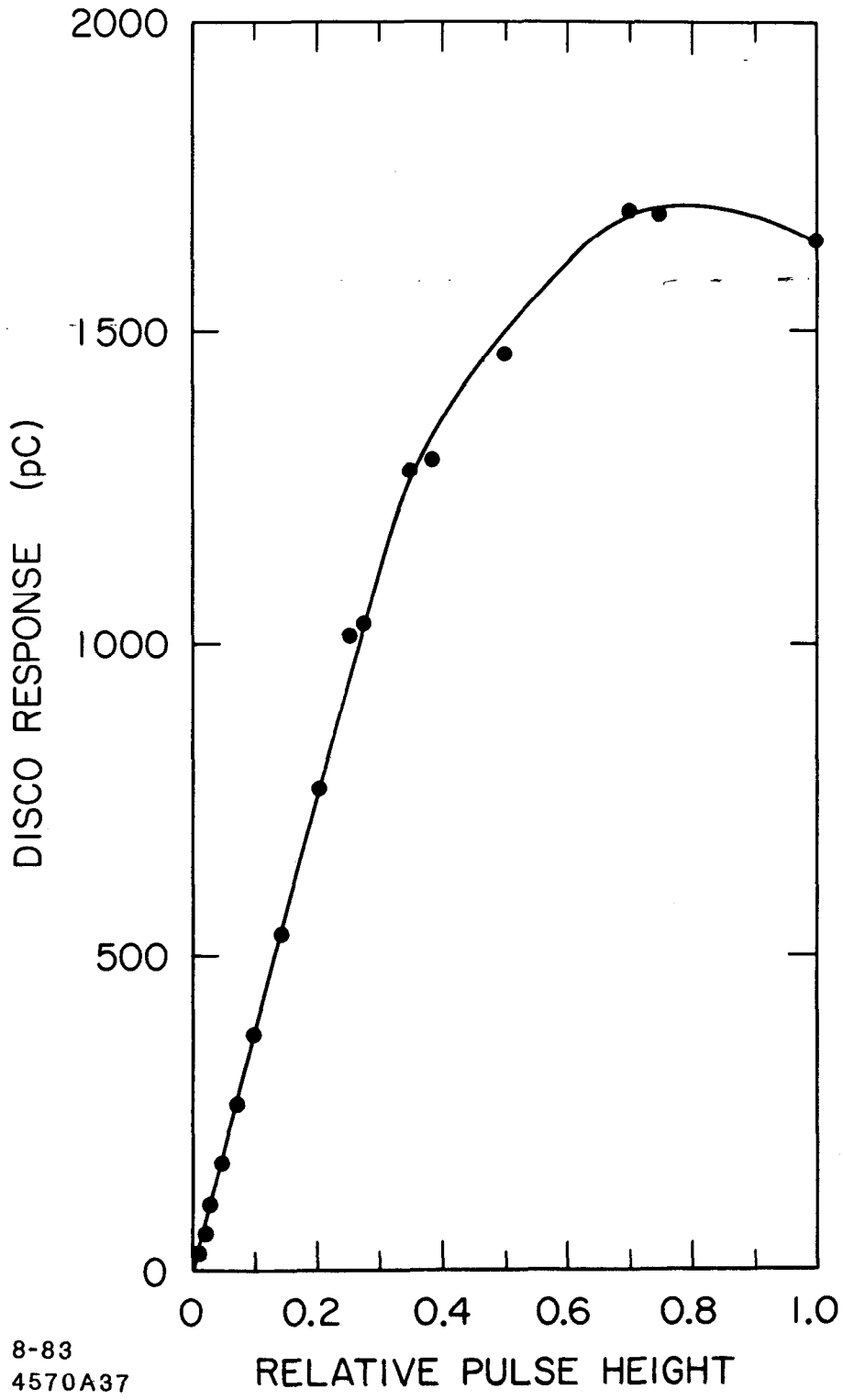
2000
1500
1000
500
0
DISCO RESPONSE (pC)
0
0.2
0.4
0.6
0.8
1.0
RELATIVE PULSE HEIGHT
8-83
4570A37

Fig. 10

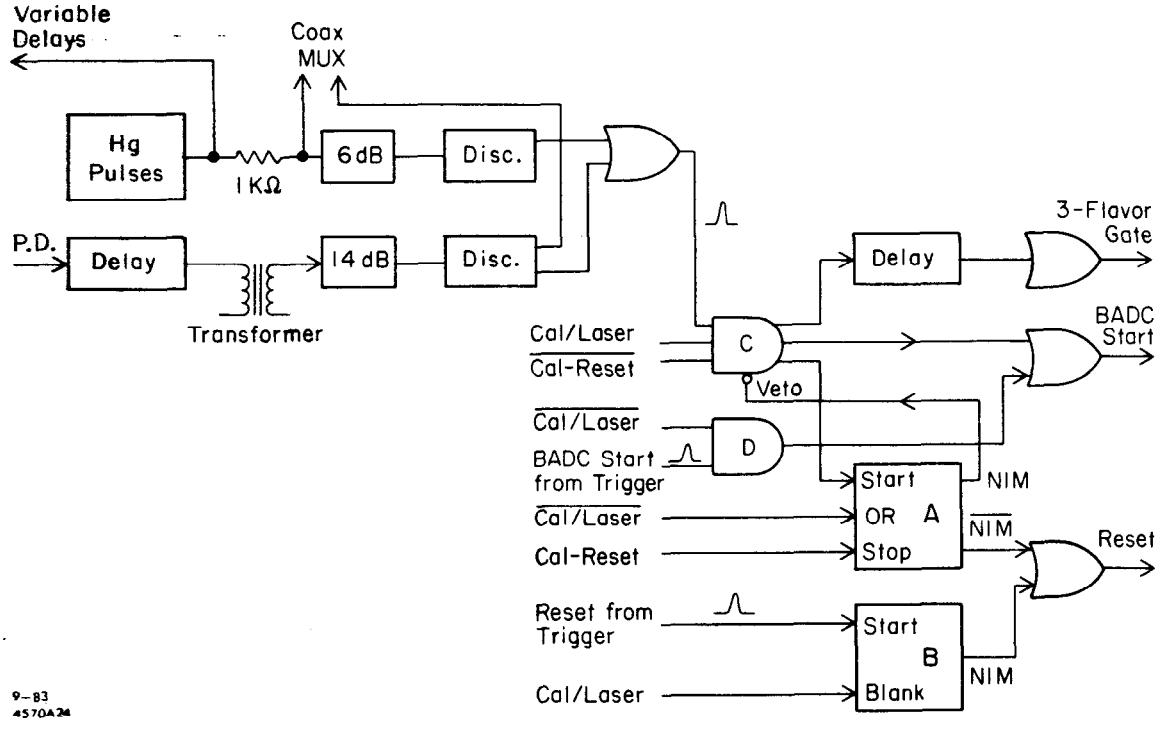
Variable Delays
Coax MUX
Hg Pulses
1KΩ
6dB
Disc.
P.D.
Delay
14 dB
Disc.
Transformer
3-Flavor Gate
Delay
BADC Start
Cal/Laser
Cal-Reset
C
Veto
Cal/Laser
BADC Start from Trigger
D
Start
OR A
Stop
NIM
Cal/Laser
Cal-Reset
NIM
Reset
Reset from Trigger
Start
B
Blank
NIM
Cal/Laser
9-83
4570A24

Fig. 11

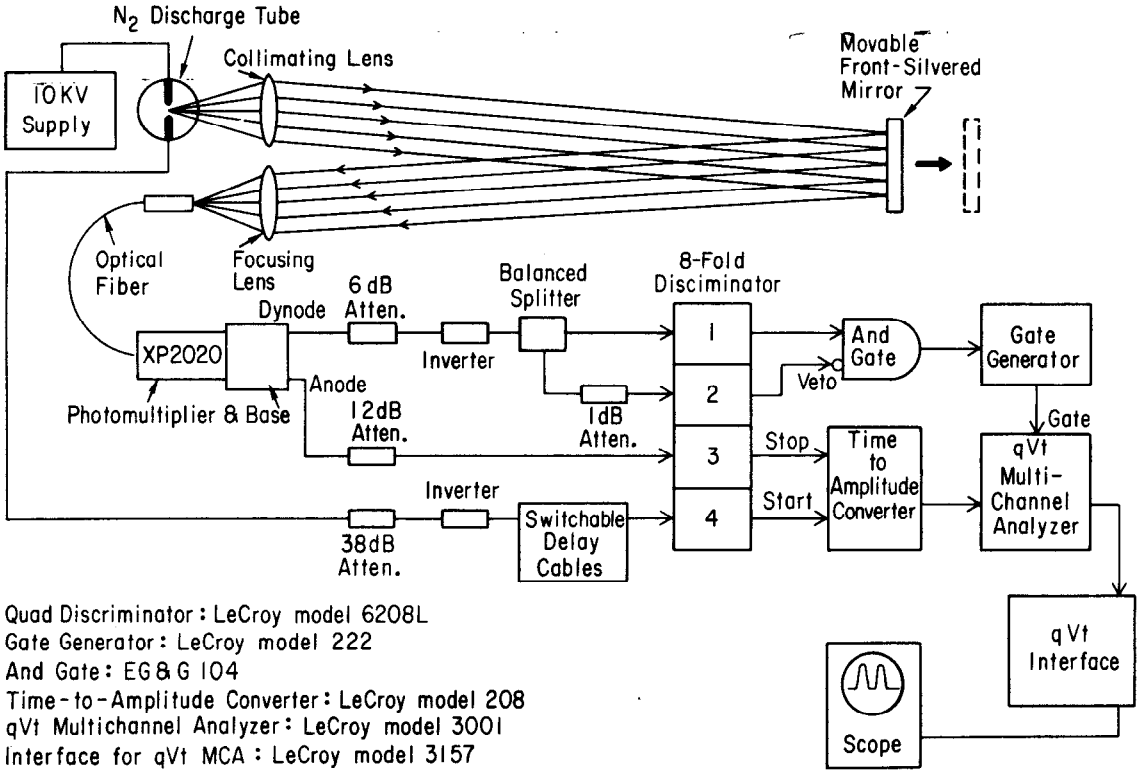

Quad Discriminator: LeCroy model 6208L
Gate Generator: LeCroy model 222
And Gate: EG&G 104
Time-to-Amplitude Converter: LeCroy model 208
qVt Multichannel Analyzer: LeCroy model 3001
Interface for qVt MCA: LeCroy model 3157

6-83 TEST SETUP FOR CALIBRATING DELAY CABLES 4570A6

Fig. 12

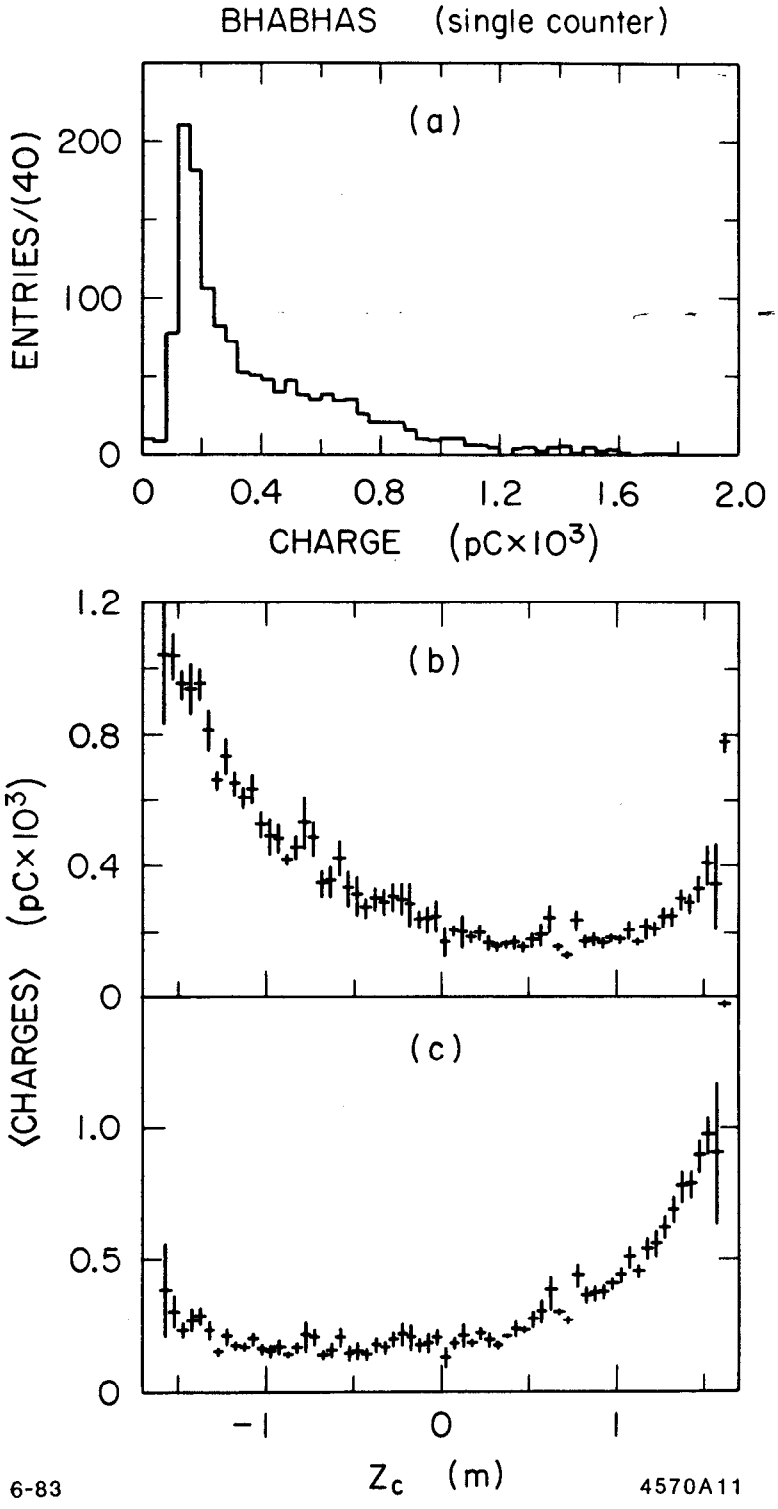
BHABHAS (single counter)
(a)
ENTRIES/(40)
200
100
0
0
0.4
0.8
1.2
1.6
2.0
CHARGE (pC×10³)
(b)
(c)
⟨CHARGES⟩ (pC×10³)
1.2
0.8
0.4
0
1.0
0.5
0
−1
0
1
Zc (m)
6-83
4570A11

Fig. 13

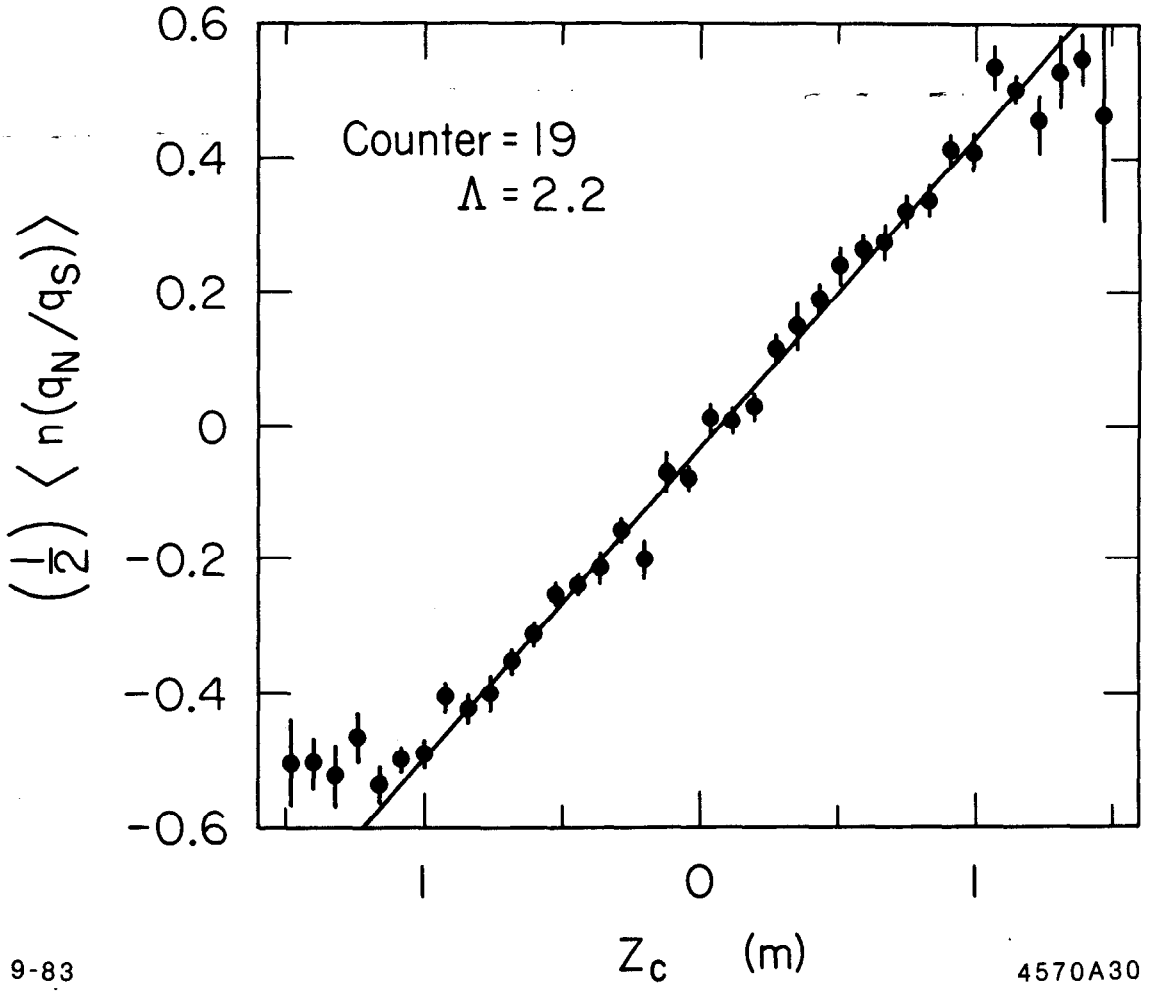

Fig. 14

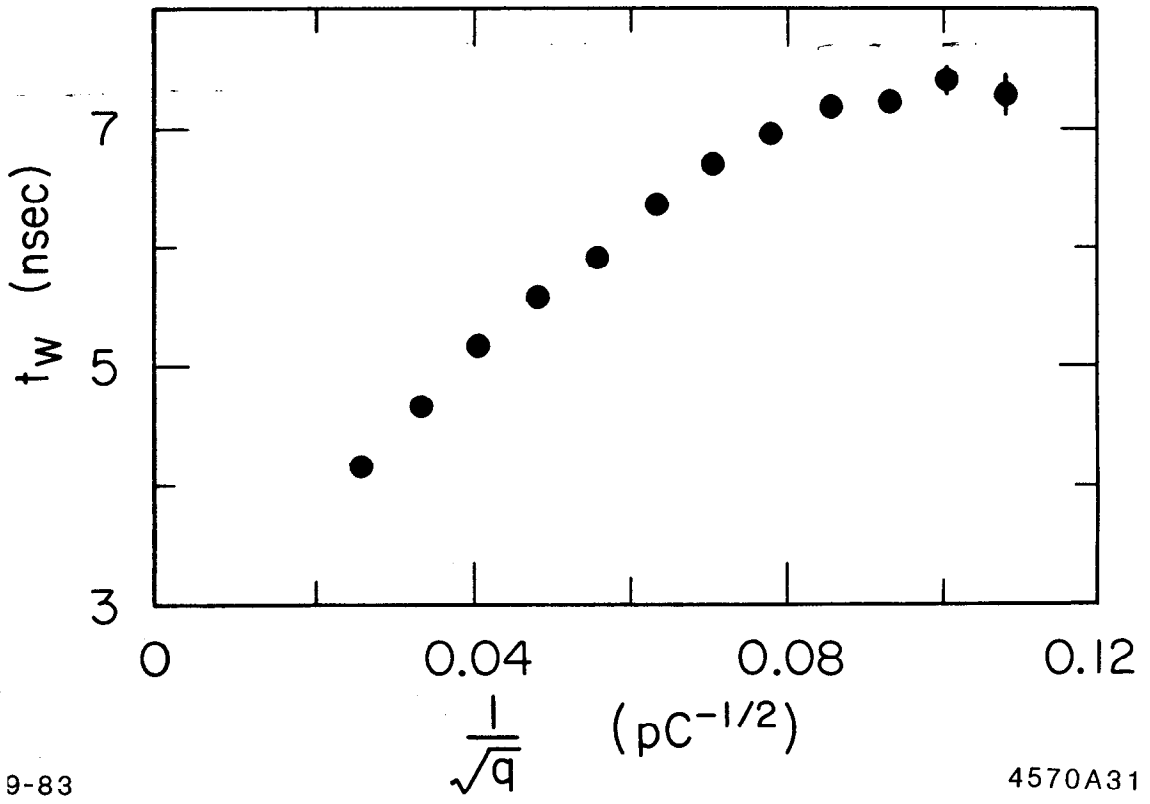

Fig. 15

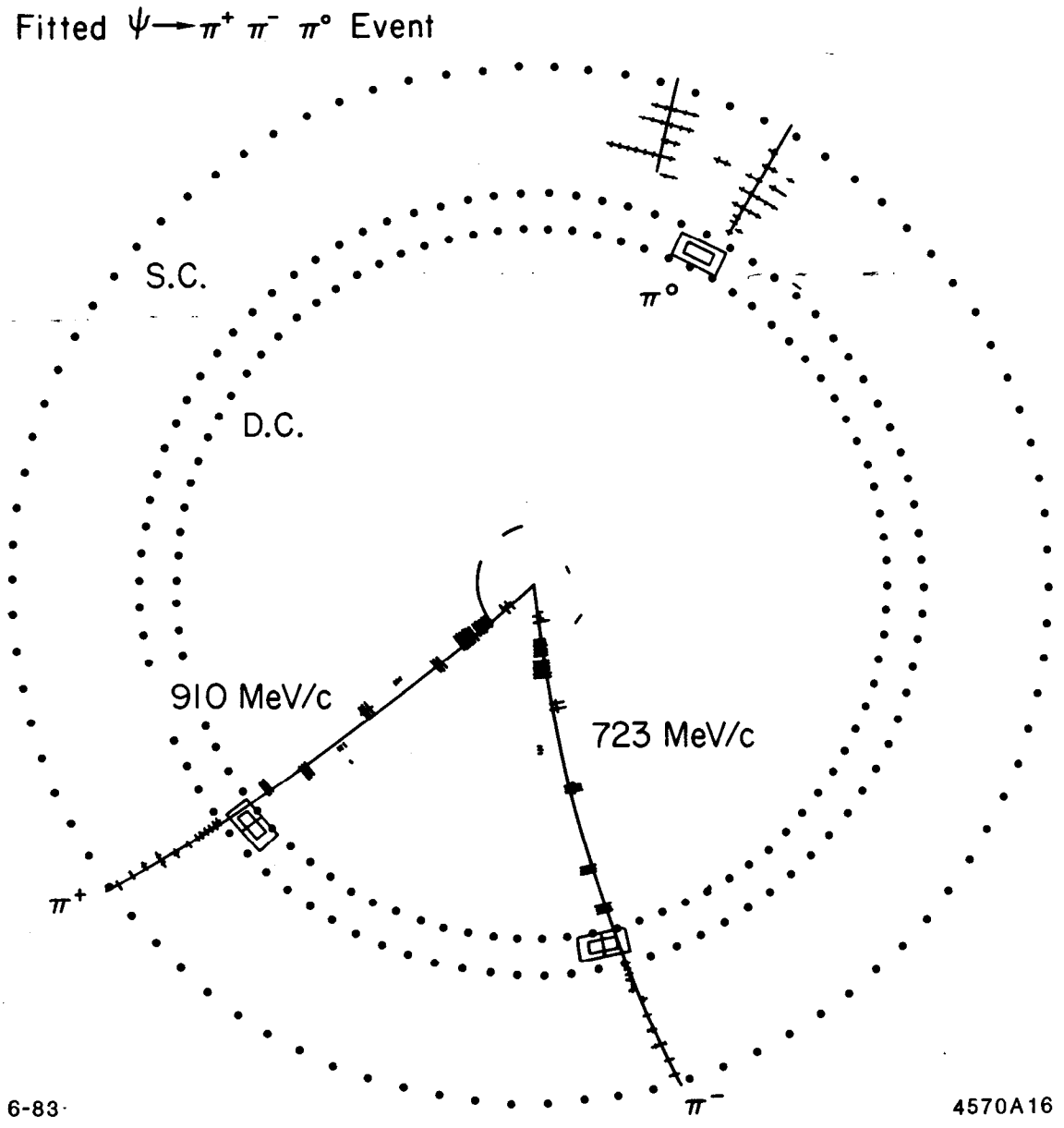
Fitted $\psi \rightarrow \pi^+ \pi^- \pi^\circ$ Event
S.C.
D.C.
π°
910 MeV/c
723 MeV/c
π^+
π^-
6-83
4570A16

Fig. 16

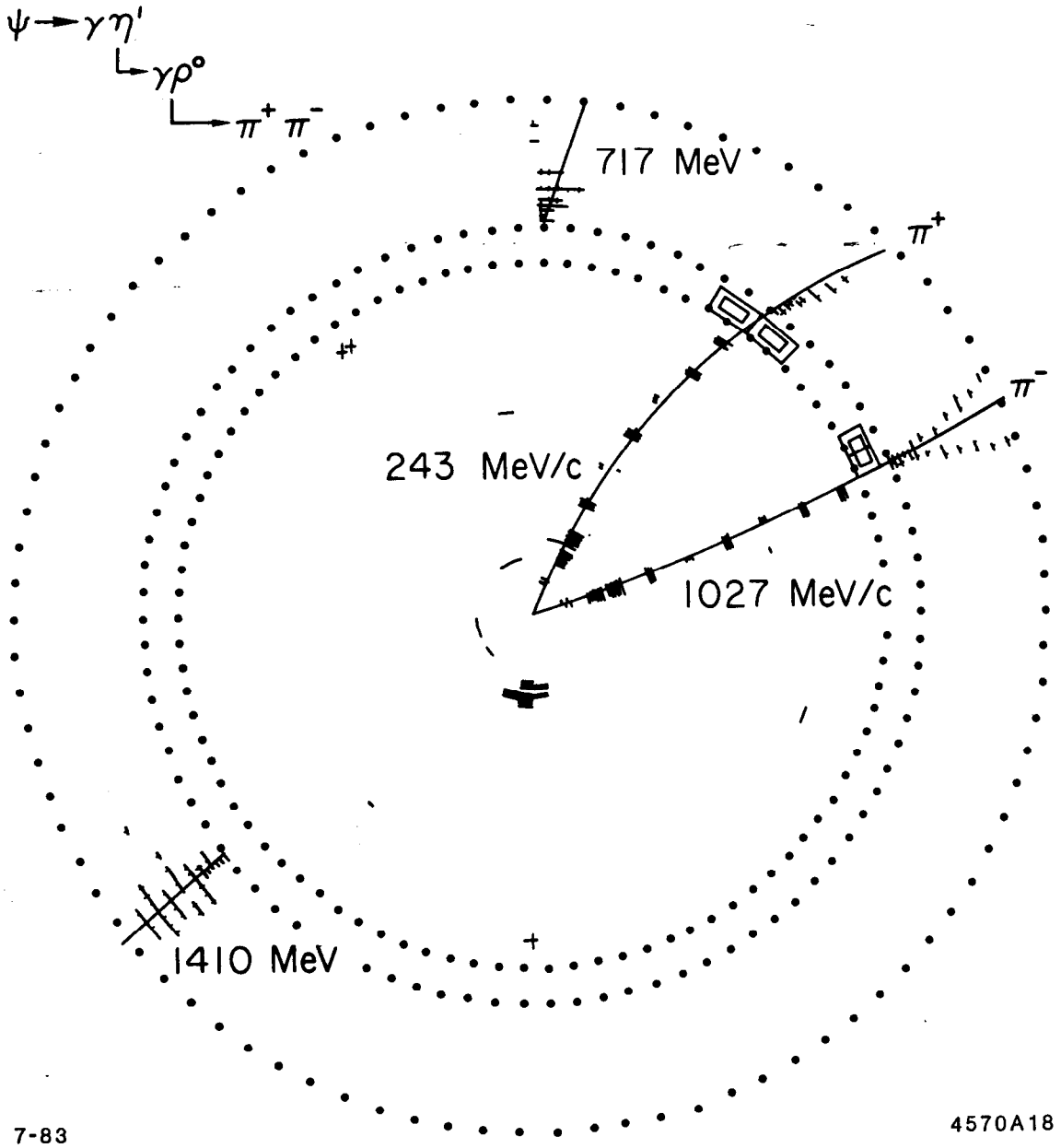

Fig. 17

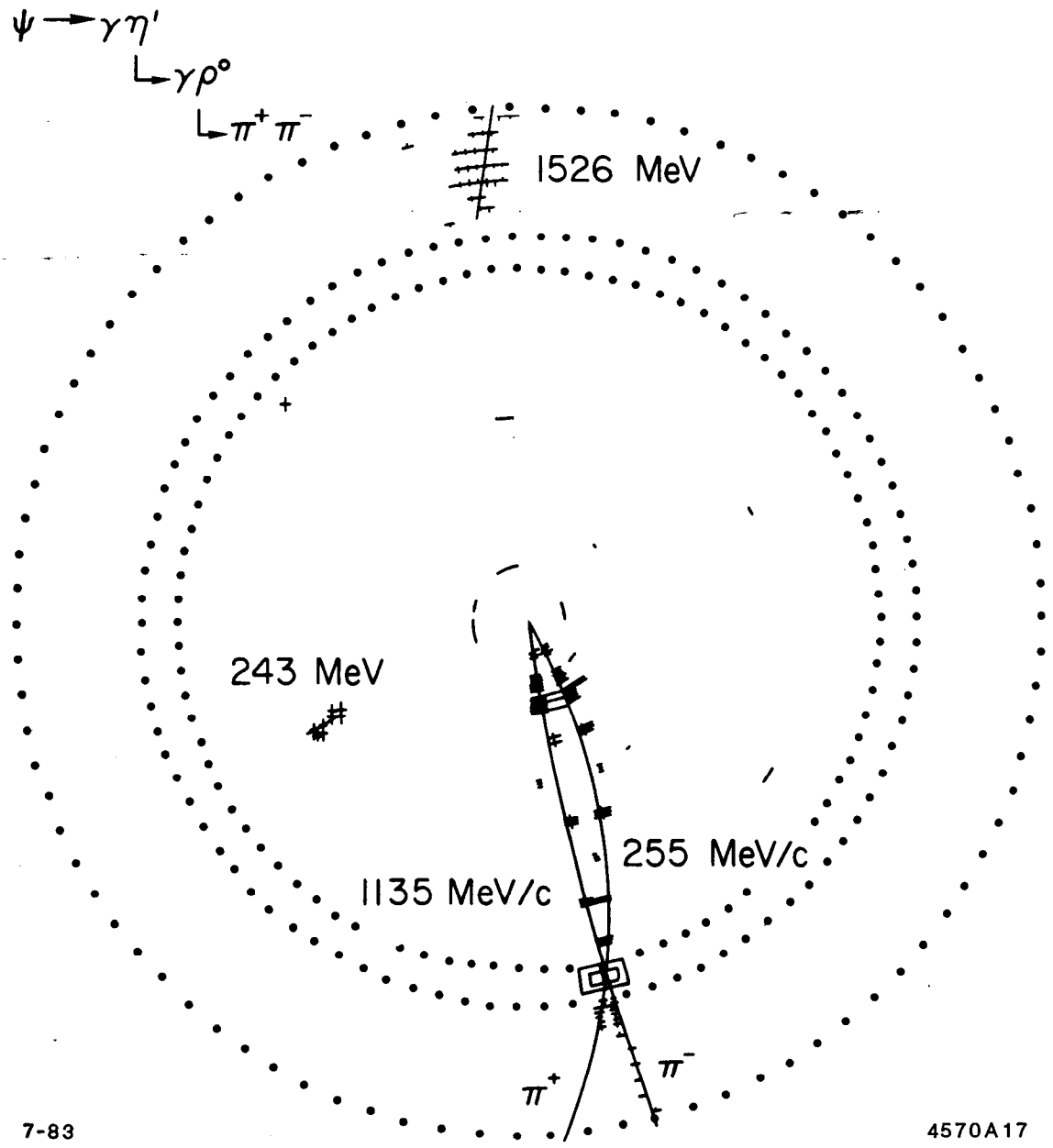

Fig. 18

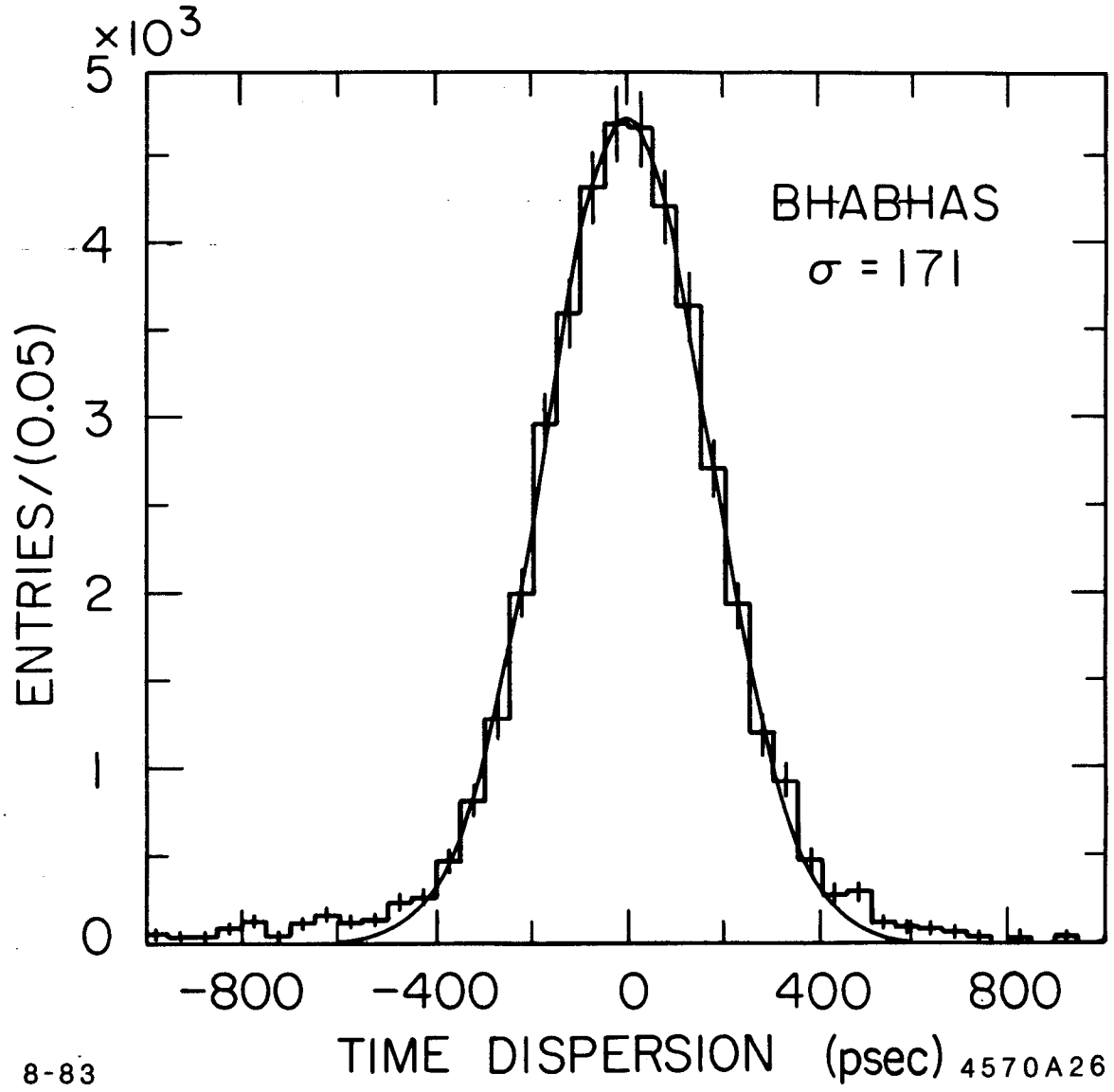
×10³
5
4
3
2
1
0
ENTRIES/(0.05)
BHABHAS
σ = 171
-800
-400
0
400
800
TIME DISPERSION (psec)
8-83
4570A26

Fig. 19

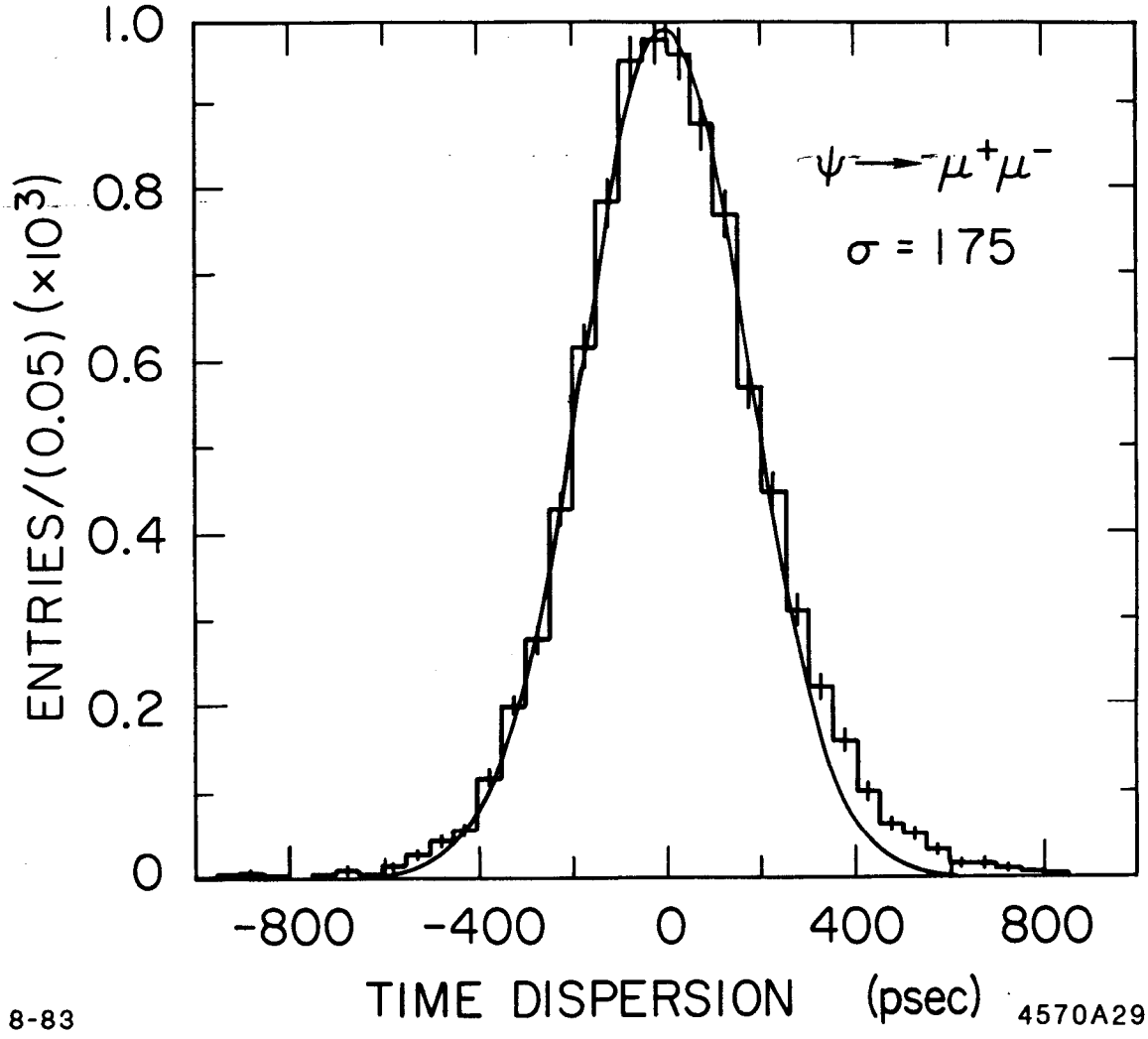
1.0
0.8
0.6
0.4
0.2
0
ENTRIES/(0.05) (×10³)
ψ → μ⁺μ⁻
σ = 175
-800
-400
0
400
800
TIME DISPERSION (psec)
8-83
4570A29

Fig. 20

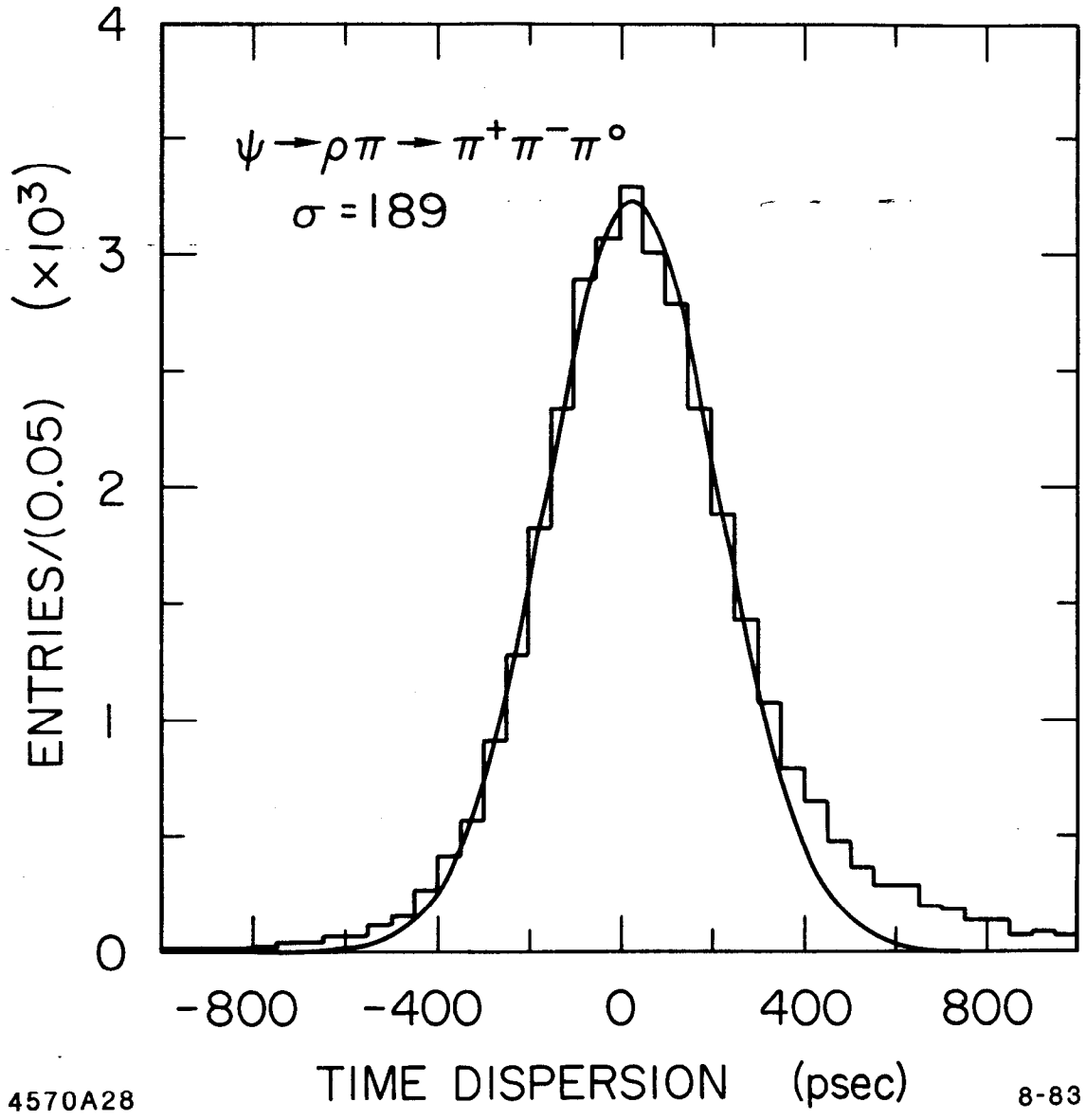
$\psi \rightarrow \rho\pi \rightarrow \pi^+\pi^-\pi^\circ$
$\sigma = 189$
ENTRIES/(0.05) (×10³)
0
1
2
3
4
-800
-400
0
400
800
TIME DISPERSION (psec)
4570A28
8-83

Fig. 21

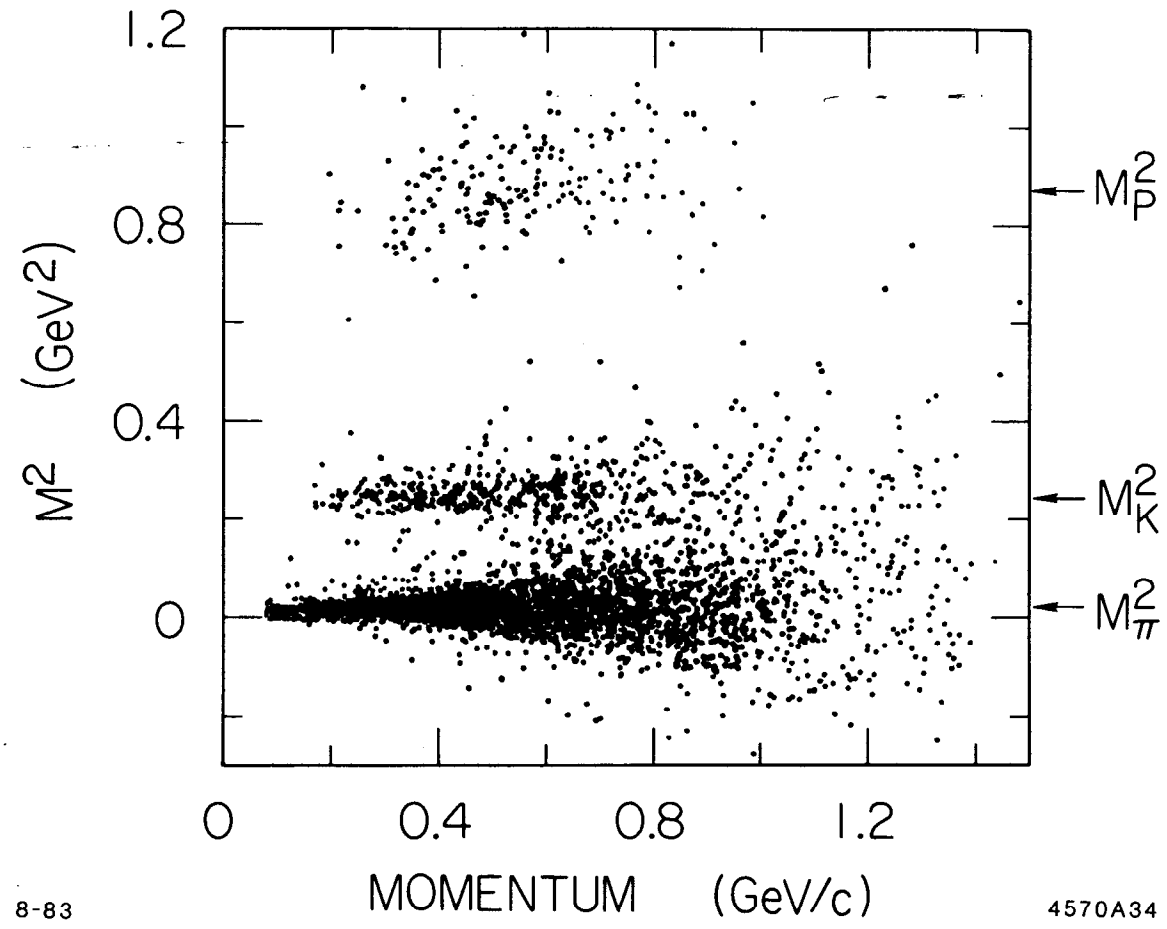
1.2
0.8
0.4
0
M2 (GeV2)
0
0.4
0.8
1.2
MOMENTUM (GeV/c)
M2P
M2K
M2π
8-83
4570A34

Fig. 22

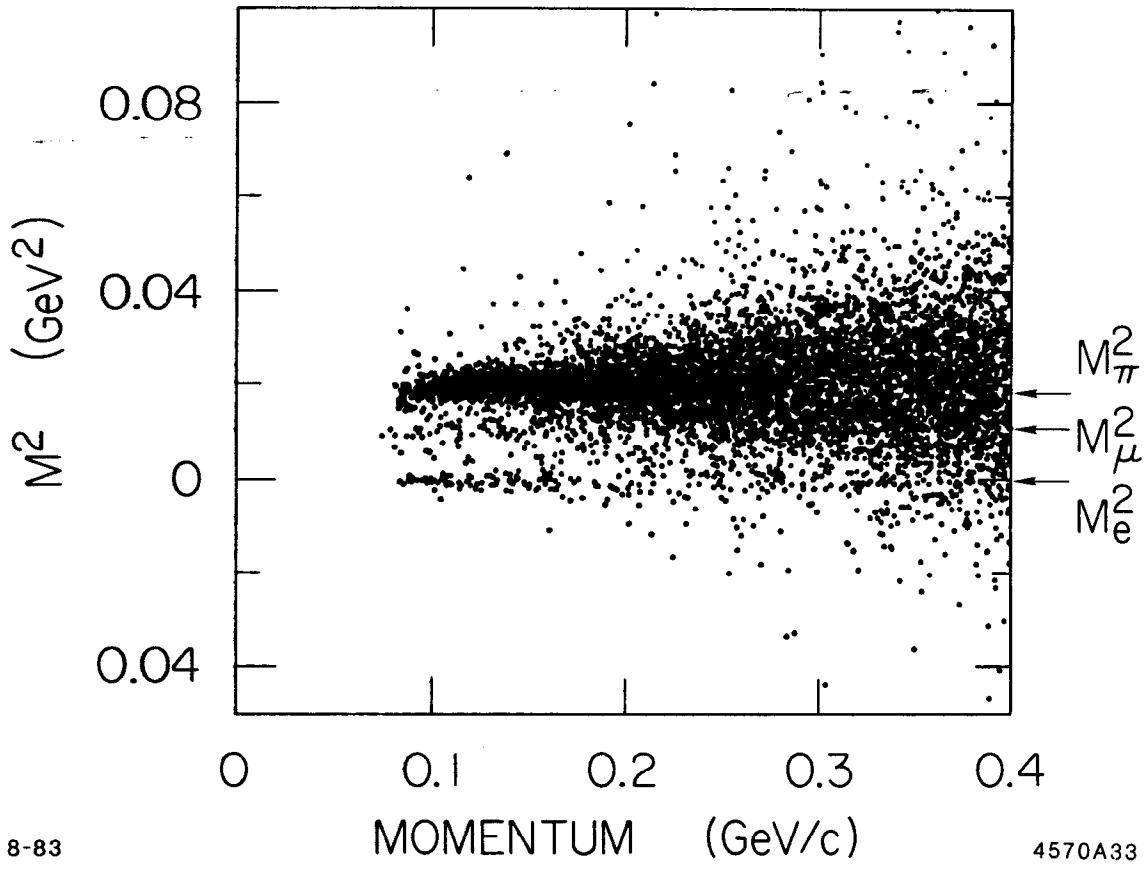
0.08
0.04
0
0.04
M2 (GeV2)
0
0.1
0.2
0.3
0.4
MOMENTUM (GeV/c)
M2π
M2μ
M2e
8-83
4570A33

Fig. 23

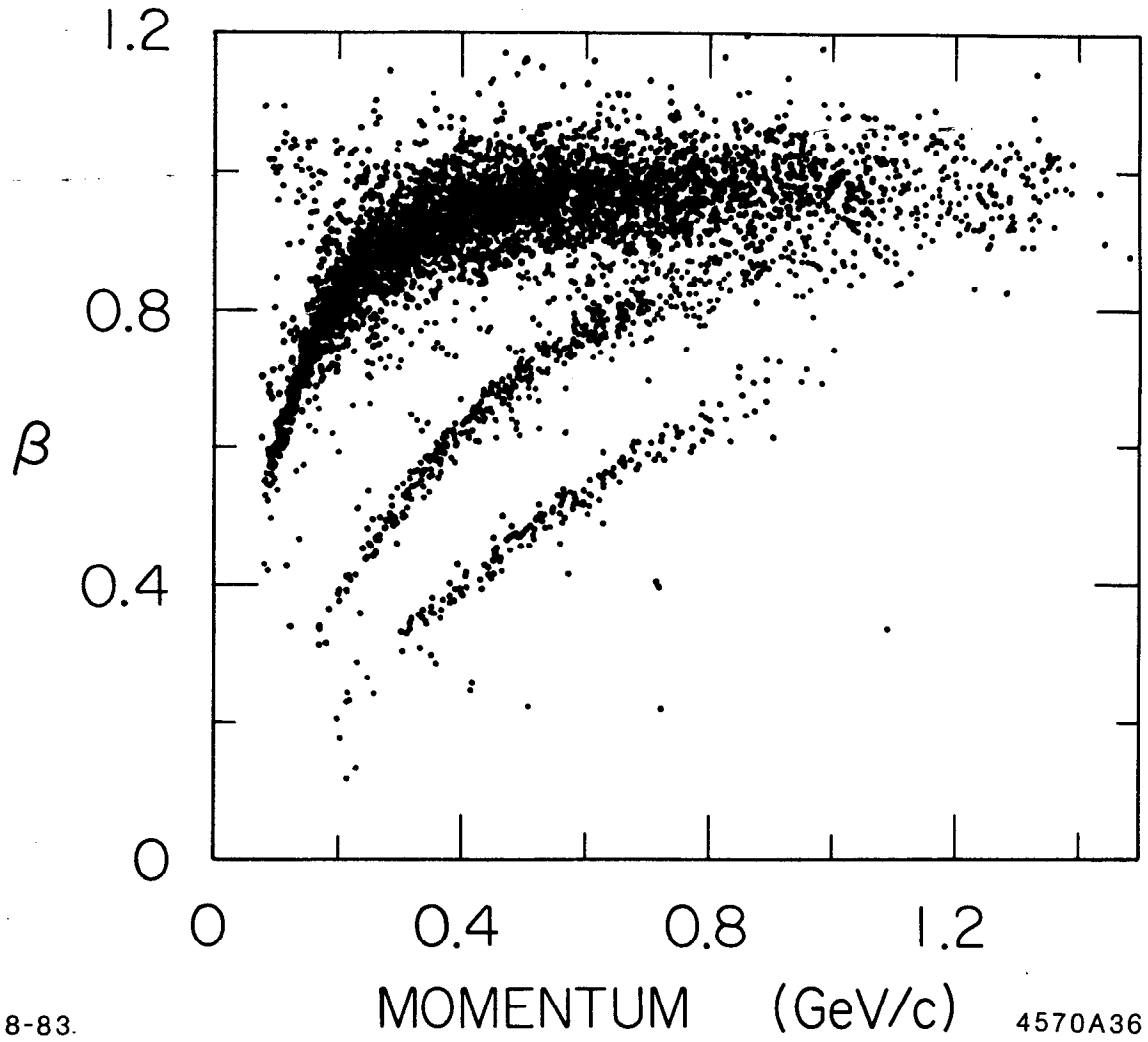

Fig. 24

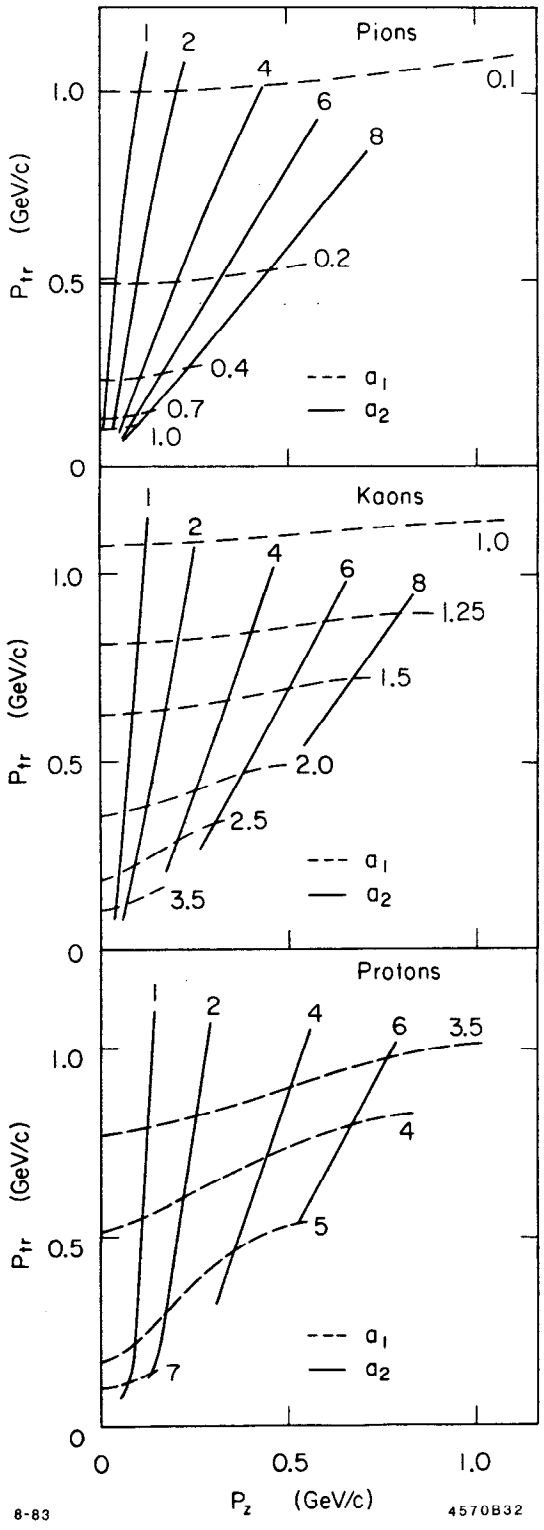
Pions
1
2
4
6
8
0.1
0.2
0.4
0.7
1.0
a_1
a_2
Kaons
1
2
4
6
8
1.0
1.25
1.5
2.0
2.5
3.5
a_1
a_2
Protons
1
2
4
6
3.5
4
5
7
a_1
a_2
P_{tr} (GeV/c)
0
0.5
1.0
P_z (GeV/c)
8-83
4570B32

Fig. 25

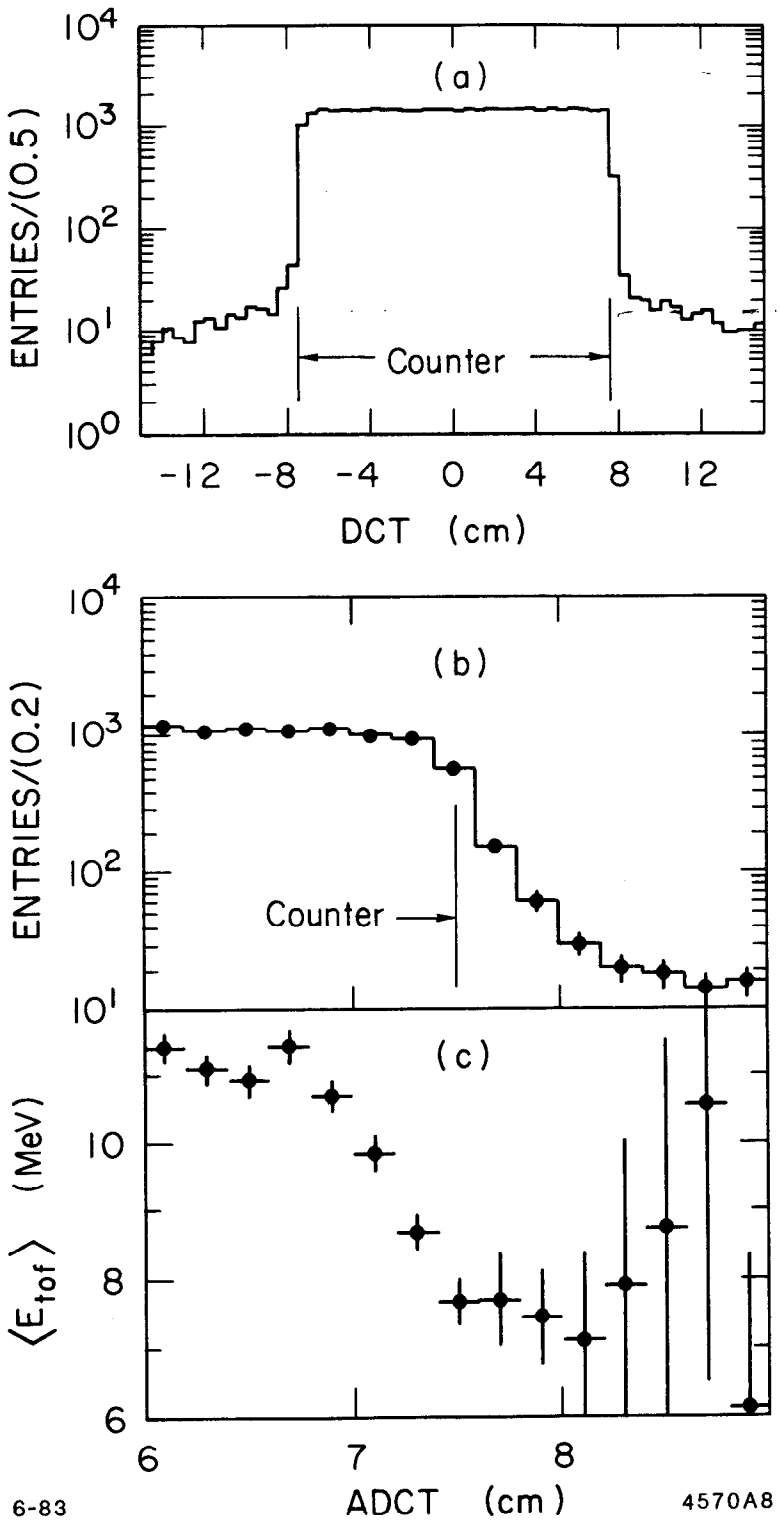
(a)
ENTRIES/(0.5)
Counter
DCT (cm)
(b)
ENTRIES/(0.2)
Counter
(c)
⟨E_tof⟩ (MeV)
ADCT (cm)
6-83
4570A8

Fig. 26

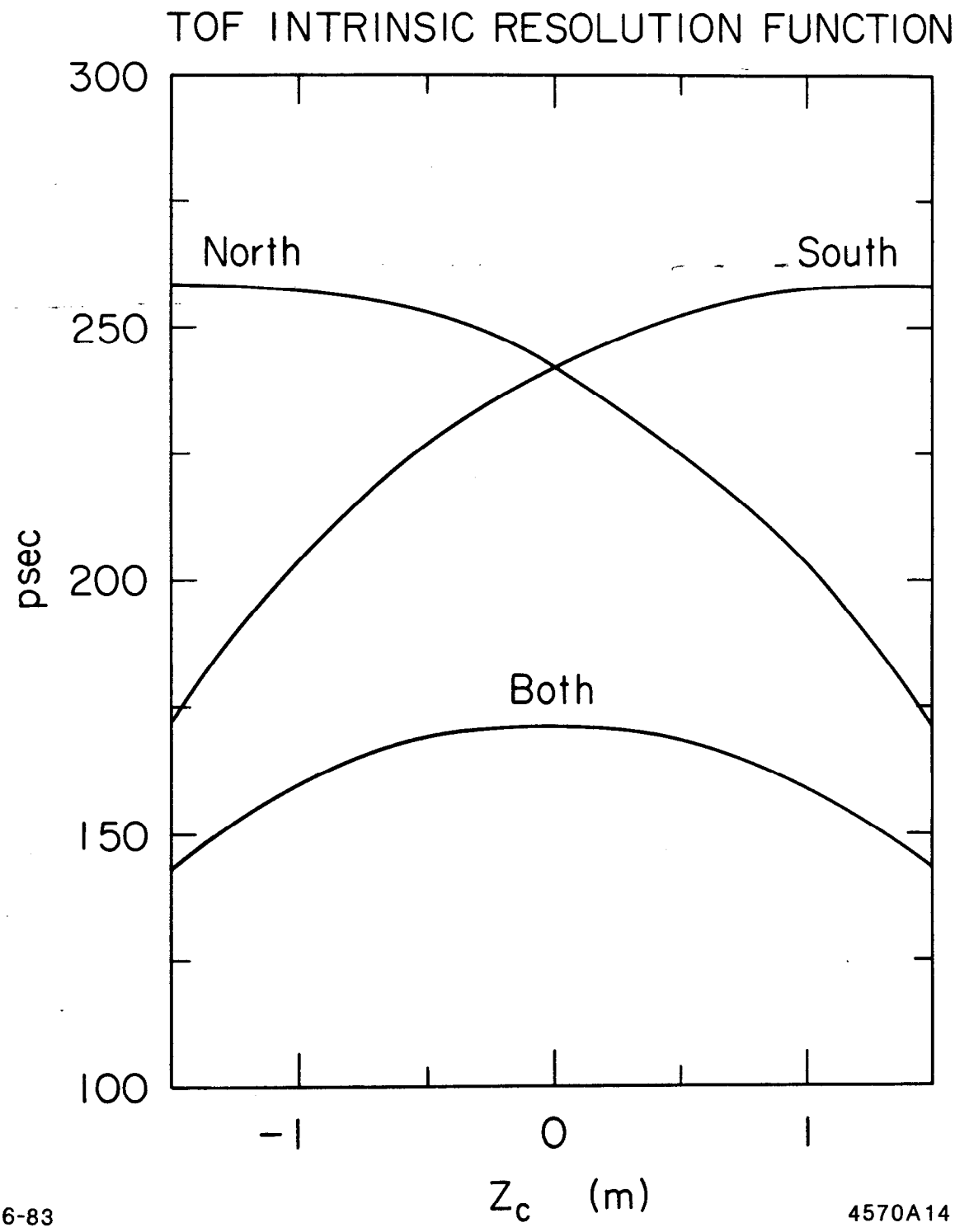
TOF INTRINSIC RESOLUTION FUNCTION
300
250
200
150
100
psec
North
South
Both
-1
0
1
Z_c (m)
6-83
4570A14

Fig. 27

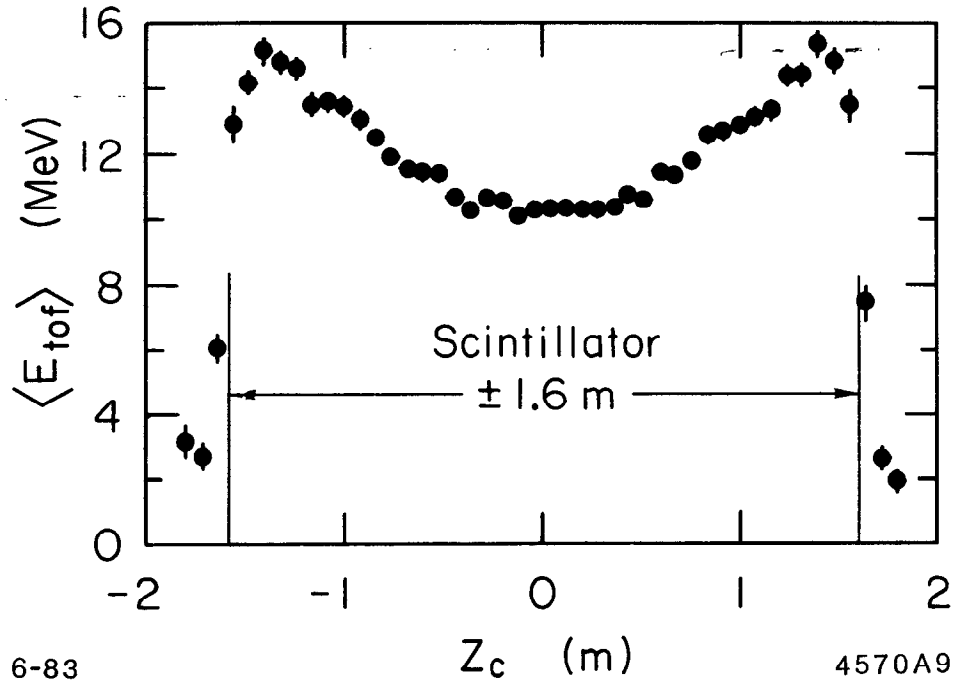

Fig. 28

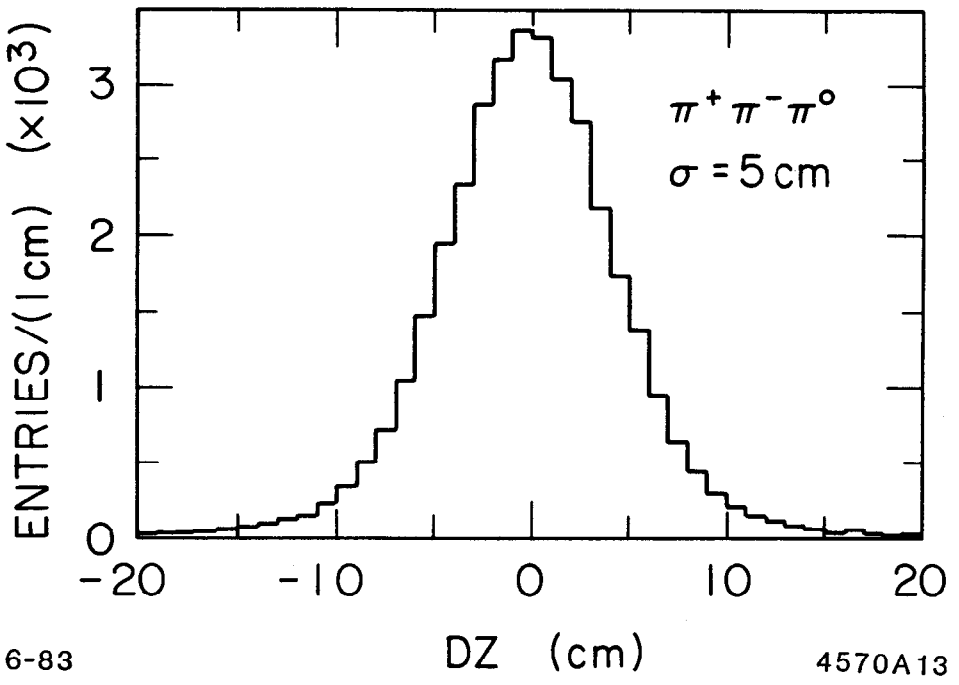

Fig. 29